Time-dependent compaction band formation in sandstone

Michael J. Heap[1], Nicolas Brantut[2], Patrick Baud[1], and Philip G. Meredith[2]

[1]*Géophysique Expérimentale, Institut de Physique de Globe de Strasbourg (UMR 7516 CNRS, Université de Strasbourg/EOST), 5 rue René Descartes, 67084 Strasbourg cedex, France.*

[2]*Rock and Ice Physics Laboratory, Department of Earth Sciences, University College London, London WC1E 6BT, U.K.*

Corresponding author: Michael Heap (heap@unistra.fr)

This article has been accepted for publication and undergone full peer review but has not been through the copyediting, typesetting, pagination and proofreading process which may lead to differences between this version and the Version of Record. Please cite this article as doi: 10.1002/2015JB012022

Abstract

Compaction bands in sandstone are laterally-extensive planar deformation features that are characterized by lower porosity and permeability than the surrounding host rock. As a result, this form of localization has important implications for both strain partitioning and fluid flow in the Earth's upper crust. To better understand the time-dependency of compaction band growth, we performed triaxial deformation experiments on water-saturated Bleurswiller sandstone (initial porosity = 0.24) under constant stress (creep) conditions in the compactant regime. Our experiments show that inelastic strain accumulates at a constant stress in the compactant regime, manifest as compaction bands. While creep in the dilatant regime is characterized by an increase in porosity and, ultimately, an acceleration in axial strain rate to shear failure, compaction creep is characterized by a reduction in porosity and a gradual deceleration in axial strain rate. The global decrease in the rates of axial strain, acoustic emission energy, and porosity change during creep compaction is punctuated at intervals by higher rate excursions, interpreted as the formation of compaction bands. The growth rate of compaction bands formed during creep is lower as the applied differential stress, and hence background creep strain rate, is decreased. However, the inelastic strain associated with the growth of a compaction band remains constant over strain rates spanning several orders of magnitude (from 10^{-8} to 10^{-5} s^{-1}). We find that, despite the large differences in strain rate and growth rate (from both creep and constant strain rate experiments), the characteristics (geometry, thickness) of the compaction bands remain essentially the same. Several lines of evidence, notably the similarity between the differential stress dependence of creep strain rate in the dilatant and compactant regimes, suggest that, as for dilatant creep, subcritical stress corrosion cracking is the mechanism responsible for compactant creep in our experiments. Our study highlights that stress corrosion is an important mechanism in the time-dependent porosity loss, subsidence, and permeability reduction of sandstone reservoirs.

Keywords: Creep; Porosity; Stress corrosion; Subsidence; Reservoir; Bleurswiller sandstone

1. Introduction

Inelastic compaction in porous sandstone formations can be manifest as discrete bands that form orthogonal to the maximum principal stress, called compaction bands (*Hill*, 1989). These geological features, in which the deformation is dominantly or purely compactant, have been documented in detail in aeolian sandstone formations in Nevada (USA, *Hill*, 1989; *Aydin and Ahmadov*, 2009; *Sternlof et al*., 2005; *Eichhubl et al.*, 2010) and Utah (USA, *Mollema and Antonellini*, 1996) and can reach tens of meters in planar extent (*Tembe et al*., 2008 and references therein). In the context of reservoirs and aquifers, the importance of compaction bands is exemplified by their substantial impact on fluid flow and reservoir compartmentalization (e.g., *Borja and Aydin*, 2004; *Sternlof et al*., 2006; *Ballas et al*., 2013; 2015; *Deng et al*., 2015). The formation of compaction bands in sandstone has also been extensively studied in the laboratory. Triaxial deformation experiments on porous sandstone samples, conducted under a constant strain rate and using a conventional triaxial stress path, have shown that compaction bands can develop over a wide range effective pressures (*Wong et al*., 1997; *Holcomb and Olsson*, 2003; *Baud et al*., 2004; *Fortin et al*., 2006; *Tembe et al.*, 2008; *Charalampidou et al*., 2011). These laboratory studies also demonstrated that inelastic compaction (i.e., permanent porosity reduction) leads to a reduction in permeability (*Wong et al*., 1997; *Zhu et al.*, 1997; *David et al.*, 2001). In all cases, a porosity reduction between 0.14 and 0.15 was seen within compaction bands formed during experiments on porous (porosity = 0.2-0.25) rocks (e.g., the porosity of a band within a rock containing a porosity of 0.2 would be between 0.05 and 0.06). More recent laboratory measurements have also shown that compaction bands in sandstone can reduce permeability by up to four orders of magnitude (*Baud et al*., 2012; *Deng et al*., 2015). After more than a decade studying compaction bands, field observations (*Schultz et al.*, 2010; *Eichhubl et al*., 2010), laboratory studies (*Louis et al*., 2007) and numerical simulations (*Katsman et al*.,

2005; *Wang et al.*, 2008) have all converged to the conclusion that the porosity and homogeneity of the host rock, and in particular the grain size distribution, are the key parameters in promoting the development of compaction bands in sandstones (*Cheung et al*., 2012).

Microcracking is the main mechanism leading to both brittle failure and compaction band formation (*Wong and Baud*, 2012). In the brittle regime (i.e., at low effective pressure and temperature), anisotropic microcracking leads to shear localization and macroscopic failure (e.g., *Lockner et al*., 1991), a process well known to exhibit a time-dependency (e.g., *Anderson and Grew*, 1977; *Atkinson*, 1982; 1984; *Atkinson and Meredith*, 1987; *Costin*, 1987; *Brantut et al*., 2013). In the presence of chemically-active pore fluids, such as water, cracks can propagate at subcritical rates assisted by fluid-rock interactions at their tips. The main mechanism postulated for such subcritical crack growth under upper crustal conditions is stress corrosion (*Anderson and Grew*, 1977; *Atkinson*, 1984). Since compaction bands in sandstone are the result of intensive microcracking and grain comminution (e.g., *Baud et al.*, 2004), it follows that their development could also be time-dependent. However, compaction bands have generally been observed to develop at relatively high effective pressures, beyond the classically-defined *brittle-ductile transition*; the importance of stress corrosion cracking at such high pressures remains unclear. Indeed, single crack experiments first designed to study this process were performed on a wide variety of rock types, at different temperatures and with different pore fluid chemistry, but all at ambient pressure (e.g., *Atkinson and Meredith*, 1987). More recently, triaxial creep experiments on sandstone (*Ngwenya et al*., 2001; *Heap et al*., 2009a; *Yang and Jiang*, 2010) focused only on the brittle (dilatant) regime and were therefore performed at low effective pressures (10 to 50 MPa). While previous studies on the compaction creep of silicate materials have focused on intergranular pressure-solution creep (e.g., *Le Guen et al*., 2007) and porosity loss in quartz aggregates (*He et al*., 2003; *Karner et*

al., 2003; *Chester et al*., 2004; *Brzesowsky et al*., 2014), laboratory studies on the growth of compaction bands in sandstone have, thus far, been restricted to experiments performed under constant strain rate conditions. To our knowledge, no previous experimental studies have been conducted on the time-dependency of compaction band growth. While it has been shown (for a variety of rocks, see *Brantut et al.*, 2013) that shear fracturing can occur over a wide range of strain rates or timescales, the motivation of this study is to investigate whether the development of compaction bands is similarly time-dependent. Could compaction bands develop over extended periods of time and at low differential stresses? Further, if compaction bands can grow during time-dependent compaction creep, are their geometrical attributes (length, thickness, and tortuosity) similar to those described previously from constant strain rate experiments? This contribution describes an experimental study in which we perform constant stress triaxial deformation experiments on porous sandstone at pressures previously shown to promote compaction band growth.

2. Materials and methods

2.1 Sample material and preparation

Bleurswiller sandstone (Bleurville, Vosges, north-eastern France) was chosen for this study because previous laboratory investigations have shown that compaction bands develop in this material when deformed at effective pressures above 60 MPa (*Fortin et al*., 2006; *Tembe et al*., 2008). It has an average connected porosity of 0.24 (±0.005), an average grain diameter of 200 μm (Figure 1), and a high permeability of 8.5×10^{-13} m^2 (measured under a confining pressure of 1 MPa), which ensures drained conditions under the experimental deformation rates reported here. Our Bleurswiller sandstone is composed of 66% quartz, 28% K-feldspar, 4% clays, and 2% mica (Figure 1). Cylindrical samples were all cored

perpendicular to bedding from a single block of material, and their end faces were then machined to ensure good parallelism. The porosity of each sample was measured using the triple weight water saturation method. All samples were vacuum-saturated with distilled water prior to experimentation.

2.2. Experimental methods

We performed two types of triaxial deformation experiment in this study: (1) constant strain rate experiments and, (2) constant stress (creep) experiments (a summary of the experimental conditions is provided in Table 1). All the experiments described in this study were performed at ambient laboratory temperature and under drained conditions. The majority of experiments were performed in the Experimental Geophysics Laboratory at the University of Strasbourg on jacketed samples 20 mm in diameter and nominally 40 mm in length. The confining and pore pressures were applied to the sample (in steps and at a rate of 0.05 MPa s^{-1}) such that the sample was never exposed to an effective pressure greater than that targeted for the experiment. The samples were left at the target effective pressure overnight to ensure microstructural equilibration.

The constant strain rate (1.0×10^{-5} s^{-1}) experiments were performed at effective pressures of 10 and 80 MPa (using a pore fluid pressure of 10 MPa). The goals of the constant strain rate experiments were twofold: (1) as a guide to the conditions to be used in later constant stress (creep) experiments and, (2) to serve as a mechanical and microstructural reference for the transition between the dilatant and compactant regimes. The creep experiments were also performed at effective pressures of 10 and 80 MPa (using a pore fluid pressure of 10 MPa). In all creep experiments, samples were first loaded at a constant strain rate of 1.0×10^{-5} s^{-1} to the target differential creep stress (guided by earlier constant strain rate experiments). Once reached, this stress was maintained constant using a servomotor and

the samples allowed to deform at constant stress for either an extended period of time (hours to days), or until shear failure ensued (in the case of the experiment at Peff = 10 MPa). Following our earlier practice (e.g., *Heap et al.*, 2009a), we also performed a stress-stepping creep experiment to investigate the stress dependence on the rate of deformation in the compactant regime. Stress-stepping creep experiments are time-efficient and also avoid any problems associated with sample variability (*Heap et al.*, 2009a). As before, the sample was loaded to the target differential creep stress at a constant strain rate of 1.0×10^{-5} s^{-1}, after which it was allowed to deform under this constant stress. Following an extended period (depending on the rate of deformation, but usually from hours to days), the differential stress was stepped up and the sample was again allowed to deform under a constant stress. This procedure was repeated for five increasing stress steps, and then, in a final step, the stress was decreased back down to the initial creep stress. To avoid damaging the samples during unloading, the samples were first unloaded at a strain rate of 1.0×10^{-5} s^{-1}, the confining and pore pressures were then reduced to room pressure at a rate of 0.05 MPa s^{-1}.

We also performed targeted complementary experiments in the 400 MPa triaxial deformation apparatus (see *Eccles et al*., 2005) at the Rock & Ice Physics Laboratory at University College London (UCL). These experiments were designed to determine the spatio-temporal distribution of acoustic emissions (AEs) to track the evolution of compaction band growth under both constant strain rate and constant stress conditions. P-wave speed evolution along different ray paths were also recorded during these latter experiments to track the progression of damage with increasing strain. Both types of experiments were performed under an effective pressure of 80 MPa (using a pore fluid pressure of 10 MPa) on jacketed samples 40 mm in diameter and nominally 100 mm in length.

During all experiments, axial stress was recorded by an external load cell and the axial shortening (strain) of the samples was measured by external linear variable differential

transformers (LVDTs). Porosity change was determined by measuring the change in pore fluid volume during experimentation, tracked by monitoring the position of the actuator inside the servo-controlled pore pressure intensifier. For the Strasbourg experiments, AE energy (the area under the root-mean-square of the received waveform) was monitored using a single piezoelectric crystal attached to the top piston. For the UCL experiments, P-wave velocities and AE locations were determined using twelve piezoelectric transducers positioned around the sample (*Eccles et al*., 2005; *Brantut et al*., 2014a). P-wave speeds were determined by regularly and sequentially sending a high frequency (about 1 MHz) and high voltage (about 250 V) pulse, that generated a mechanical wave with a known origin time, to each of the twelve transducers. The remaining eleven recorded the arrival time of the generated waveform. Precise P-wave arrival times were determined using a cross-correlation technique (further details can be found in *Brantut et al*., 2014b). The positions of the transducers around the sample allowed P-wave speeds to be calculated in four directions relative to the sample axis: 90°, 58°, 38.7°, and 28.1°, respectively (see *Brantut et al*., 2014a for further details). The twelve transducers were also used to locate AE events. AEs were located using the arrival times of waveforms generated by microcracking events within the sample to the twelve transducers and a homogenized transversely isotropic P-wave speed model (*Thomsen*, 1986) that uses P-wave speeds interpolated in time from the measured values.

3. Results

3.1 Constant strain rate experiments

Stress-strain curves for constant strain rate experiments at effective pressures of 10 and 80 MPa (pore fluid pressure = 10 MPa) are presented in Figures 2a and 2b, respectively,

while Figures 2c and 2d show the associated evolution of porosity as a function of axial strain for the same experiments. The deformation behaviour at an effective pressure of 10 MPa (Figures 2a and 2c) can be described as dilatant. The approach to sample failure, manifest as a shear fracture orientated at about 30° to direction of loading (Figure 3a), is characterized by an increase in porosity (dilatancy; Figure 2c) and an acceleration in the output of AE energy (Figure 2a). The onset of dilatational microcracking (termed C'), determined using a combination of the onset of AE activity and a change in the rate of porosity reduction, occurred at a differential stress of about 40 MPa (marked by an arrow on Figure 2a), and macroscopic sample failure (shear fracture formation) occurred following the peak stress (σ_p); the peak stress occurred at a differential stress of 72 MPa and an axial strain of about 1% (sample failure and the peak stress are also marked by arrows on Figure 2a). By contrast, the deformation behaviour at an effective pressure of 80 MPa (Figures 2b and 2d) is entirely compactant. The stress-strain curve shows no strain softening; rather, inelastic strain hardening is seen to commence at about 5% axial strain after which stress and strain increase more or less linearly. The onset of shear-enhanced compaction (termed C*), determined using the porosity reduction data, occurred at a differential stress of about 45 MPa (marked by an arrow on Figure 2b; see also Table 1). Prior to strain hardening, the stress-strain curve is punctuated by small stress drops that are associated with small accelerations in the output of AE energy (Figure 2b). We also note that the overall output of AE energy decelerates during strain hardening (Figure 2b), as previously observed during the inelastic compaction of porous sandstone (*Wong et al*., 1997; *Ingraham et al*., 2013).

To track the development of compaction band growth during evolving deformation, we performed experiments at an effective pressure of 80 MPa to axial strains of 1.5, 3, and 13% (marked by the filled circles on Figure 2b). Compaction bands are universally observed in our deformed and recovered samples: one compaction band and 2-3 compaction bands in

the samples deformed to 1.5% and 3% axial strain, respectively (Figures 3b and 3c). At an axial strain of 13.5%, the recovered sample contained many compaction bands (Figure 3d). The differences between deformation characteristics in the dilatant and compactant regimes is exemplified by the large differences in the ranges of stress, strain and porosity change seen in the axes of the plots in Figure 2; for comparison, synoptic plots showing the stress-strain curves and the porosity reduction curves for both regimes on the same axes are provided as insets in Figures 2b and 2d, respectively.

We performed a complementary constant strain rate experiment under an effective pressure of 80 MPa (pore fluid pressure = 10 MPa) to 5% axial strain in which we recorded both the spatio-temporal evolution of AE locations and the evolution of P-wave speeds (Figure 4). Stress and porosity reduction are plotted as functions of axial strain in Figure 4a, the evolutions of P-wave speeds versus axial strain are shown in Figure 4b, and the locations of AE events are provided in Figure 4c for the strain intervals (a – g) indicated on Figures 4a and 4b. As for the earlier experiments at an effective pressure of 80 MPa (Figure 2b), the mechanical response of the rock was entirely compactant: We observe no strain softening, but a continuous reduction in porosity during deformation (Figure 4a). Our data also show that, as strain increases, P-wave speeds decrease in all four measured directions (Figure 4b). For example, at an angle of 90° to the sample axis, the P-wave speed reduced by approximately 11%, from about 3.7 to about 3.4 km s^{-1}. In detail, the total decrease in P-wave speed was most pronounced in the radial direction (90°) and decreased in sequence as the angle from the sample axis decreased (Figure 4b). The AE locations highlight that the deformation became localized in bands orientated sub-perpendicular to the direction of the maximum principal stress. We observe that the first compaction band initiated during strain interval (c) (Figure 4c, indicated by an arrow), after the stress begins to plateau at about 2% axial strain and a differential stress of about 100 MPa (Figure 4a). This band grows across the sample during

strain interval (d). The growth of at least two new compaction bands can be identified in strain intervals (e) and (g) (indicated by arrows). Although the AE locations are diffuse during strain interval (g), we infer this to be the result of a number of compaction bands growing simultaneously. Indeed, many compaction bands were observed in the retrieved sample. The AE location data of Figure 4c are comparable to those from similar experiments performed on Bleurswiller sandstone presented in *Fortin et al*. (2006).

3.2 Constant stress (creep) experiments

The stress-strain curves from our constant stress (creep) experiments are plotted in Figure 5 together with the curves from our earlier constant strain rate experiments for comparison. Firstly, our creep data show that strain can accumulate at constant stress in the dilatant regime (at an effective pressure of 10 MPa; Figure 5a), as also demonstrated previously for many rock types (see *Brantut et al.*, 2013 for a review). In the dilatant regime we observe that shear failure under-constant stress occurs at approximately the same value of strain as for the constant strain rate experiment, in spite of the fact that this strain was accumulated much more slowly in the creep experiment, over a period of 800 minutes, compared to less than 20 minutes in the constant strain rate experiment (Figure 5a; see also *Brantut et al.*, 2013). Our creep experiments at an effective pressure of 80 MPa reveal that strain can also accumulate at constant stress in the compactant regime (Figure 5b). In particular, our experiments show that compaction creep is observed between the stress level of C* and the plateau stress defined by our constant strain rate experiment (Figure 5b). At the highest level of applied creep stress (90 MPa; close to the constant strain rate stress plateau), 4.5% of creep strain was accumulated in about 1500 minutes, whereas at the lowest applied creep stress (60 MPa; closest to the stress level of C*), it took much longer, about 4000 minutes, to accumulate a significantly smaller creep strain of only 0.2%.

Figures 6a and 6c show the evolution of axial creep strain and AE energy output as functions of time, and porosity reduction as a function of time, for the constant stress portion of the creep experiment performed in the dilatant regime (Peff = 10 MPa), respectively. Although brittle creep experiments have been well documented in the literature (*Brantut et al.*, 2013 and references therein), we present these data here, and explain the characteristics of brittle creep, in order to highlight the key differences between creep in the dilatant and compactant regimes. During brittle creep, the rates of axial strain, AE activity, and porosity reduction first decrease and then gradually increase until sample failure ensues (Figure 6a and 6c). The porosity reduction curve shows that the sample is dilating throughout brittle creep (Figure 6c). Failure of the sample is manifest as a localized shear fracture orientated at about 30° to direction of loading, as shown in the inset on Figure 6a. This behaviour is typical of brittle creep in rocks and has previously been observed for many rock types, including sandstone (*Ngwenya et al.*, 2001; *Heap et al.*, 2009a), basalt (*Heap et al.*, 2011), granite (*Fujii et al.*, 1999), and limestone (*Brantut et al.*, 2014b).

Figures 6b and 6d show the evolution of axial creep strain, AE energy, and porosity reduction as functions of time for one of our creep experiments performed in the compactant regime (Peff = 80 MPa and Q = 90 MPa). It is clear that compaction creep differs significantly from creep in the dilatant regime. In contrast to dilatant creep, we do not observe a final phase of acceleration in strain rate, AE activity, or porosity change during compaction creep. Rather, we observe a continuous, decelerating accumulation of strain throughout (Figure 6b). We also note that the recovered sample deformed at a differential stress of 90 MPa in the compactant regime contained many compaction bands, as shown in the inset on Figure 6b. The large differences between the axes of the graphs in Figure 6 exemplify the large differences between creep in the dilatant and compactant regimes. For example, over a time interval of 800 minutes, compaction creep produced an axial strain of

3.5% and a porosity decrease of 0.035, while dilatant creep produced an axial strain of only 0.25% strain and a porosity increase of 0.0025.

On closer inspection of Figures 6b and 6d, we notice that the global decelerations in axial strain, AE activity, and porosity reduction are not entirely smooth, but are punctuated by several higher rate excursions. These excursions are more easily seen when the same data are plotted as rates of change against time, as shown in Figure 7. The rate data of Figure 7 show that the excursions in all three independently measured parameters occurred simultaneously. Such excursions are much more pronounced in experiments performed at lower differential stress (and thus lower background strain rate). This is illustrated in Figure 8, which shows the evolution of strain, AE energy, and porosity reduction with time (Figure 8a), and their rates of change against time (Figure 8b), for an experiment performed at the same effective pressure of 80 MPa, but a lower differential stress of 80 MPa. Two excursions from the baseline are observed in all three parameters in this five day long experiment, with each lasting approximately 20 hours (Figure 8b). The first excursion commenced around 2000 minutes and is associated with a temporary increase in axial strain rate of about an order of magnitude. The second excursion, starting around 4500 minutes, was much smaller in amplitude and associated with an increase in strain rate of only a factor of two to three. Visual inspection of the recovered sample after deformation showed that it contained two discrete compaction bands, one broad and one narrow, as shown in the inset on Figure 8a.

The spatio-temporal evolution of microcracking during compaction creep at an effective pressure of 80 MPa and a creep stress of 92.2 MPa is presented in Figure 9. In agreement with our earlier experiments under very similar conditions (Figures 6b and 6d), we observe that strain accumulated and porosity decreased throughout the constant stress phase (Figure 9a). The evolution of P-wave speeds with increasing strain during the experiment is shown in Figure 9b. We observe that the P-wave velocities in all measured directions

decreased during compaction creep (Figure 9b; strain intervals b – g). For example, the radial P-wave speed, along the direction normal to the sample axis, was reduced by about 0.2 km s^{-1}, from 3.6 to 3.4 km s^{-1}. The reductions in P-wave speed measured under constant stress conditions are quantitatively similar to those measured during the constant strain rate experiment (Figure 4b) which was taken to a similar total axial strain and, in both cases, the overall decrease in P-wave speed was higher for orientations at higher angles to the sample axis (Figures 4b and 9b). Again, we observe a number of excursions in the axial strain and porosity reduction rates during compaction creep (plotted in Figure 9c), with the clearest occurring during strain interval (e). The AE locations determined during this experiment (Figure 9d) show that discrete bands, orientated sub-perpendicular to the direction of loading, formed during compaction creep. We notice that the first band traverses the sample by the end of strain interval (b) (indicated by arrows); AE events are also located along this band in strain interval (c) and (d). We also observe the emergence of two new bands during strain interval (c) (indicated by arrows), one of which grows across the sample during strain interval (d) (indicated by arrows). A significantly broader band grows across the center of the sample (indicated by arrows) during strain interval (e), the same interval where the largest excursions in strain rate and porosity reduction rate are observed in Figure 9c. Further bands continue to grow with increasing deformation, such that by the end of the experiment the located AE events form a diffuse cloud covering the central portion of the sample and individual bands can no longer be distinguished. Again the retrieved sample shows evidence of multiple compaction bands during post-test visual inspection, as shown in the far right image of Figure 9d.

The results from the stress-stepping creep experiment are presented in Figure 10. The stress-strain curve for this experiment, which lasted for approximately 7 days, is shown in Figure 10a, together with the curve for the constant strain rate experiment of Figure 2b (in

which 4% strain was achieved in about 60 minutes), for comparison. In the stress-stepping test, the differential stress was first increased to 85 MPa, after which the creep stress was sequentially stepped up to 90, 92.5, 95, 97.5, and 100 MPa. As a final step, the differential stress was stepped back down to 90 MPa. Figure 10b shows the evolution of the axial strain rate and porosity reduction rate during the experiment. Note that the first vertical panel in Figures 10a and 10b marks the initial loading to 85 MPa at constant strain rate, prior to the first creep phase of the experiment. The spikes in both signals (strain and porosity reduction rate) at the start of each stress step are associated with the imposed stress increase, and therefore do not correspond to creep deformation. Overall, the general trend between these spikes is for higher differential stresses to produce higher creep strain rates and porosity reduction rates. However, similarly to the earlier experiments, creep at each stress level is again interrupted by excursions in the strain and porosity reduction rates of variable amplitude and duration. The observation that higher creep strain rates are associated with higher differential stresses can be better illustrated by plotting computed creep strain rates for each stress level against the differential stress, as done in Figure 11. Overall, we find that a 10 MPa increase in differential creep stress results in an increase of two orders of magnitude in the creep strain rate. In the final phase of the experiment, the differential stress was stepped back down from 100 to 90 MPa. We note from Figure 11 (open circles) that this reduction in stress resulted in a significant reduction in creep strain rate, almost back (within about a factor of two) to the rate associated with this stress level during the first upward stress step.

3.3 Microstructural observations

We performed post-mortem microstructural analysis on samples containing compaction bands formed under both constant strain rate (to 3% axial strain; see Figure 2b) and constant stress conditions (Q = 80 MPa; the experiment shown in Figure 8) using a

scanning electron microscope (SEM). Our goal here was to see whether compaction bands formed relatively rapidly at constant strain rate were microstucturally distinct from those formed much more slowly during time-dependent creep at constant stress. Our microstructural observations are summarized in Figure 12, complemented by a micrograph of the intact material for comparison. We find that compaction localization produced under a constant strain rate (Figure 12b) comprises bands of comminuted grains with a mean thickness of about 2-3 intact grain diameters (intact grain diameter = 0.2 mm), similar to those previously observed in Bleurswiller sandstone (e.g., *Fortin et al*., 2006). Two deformation bands were formed in the constant stress experiment shown in Figure 8, a narrow band (about 0.5 mm wide) close to the top of the sample and a broader band (1-2 mm wide) in the center of the sample (see inset in Figure 8a). The narrow band comprises a discrete, tortuous compaction band of comminuted grains, and is shown in Figure 12c. By contrast, the broader band comprises an array of band segments, each approximately 0.5 mm wide (a photomicrograph of this broader band can be found in Figure 14b). In summary, we find no discernible difference between the characteristics of the compaction bands formed under the different experimental conditions. We note that all of the deformation is localized within the bands, with no significant microcracking observed in the remainder of the sample.

4. Discussion

4.1 The growth of creep compaction bands

Our experiments clearly demonstrate that creep deformation can occur in the compactant regime and, in the case of Bleurswiller sandstone, is characterized by the growth of compaction bands (Figures 6b and 12c). In detail, the gradual reduction in creep rate during compaction creep is accompanied by higher rate excursions from the underlying

baseline trend in the rates of axial strain, AE energy, and porosity reduction (Figures 7 and 8). This is particularly clear for the experiment with a low baseline creep rate shown in Figure 8 in which we observe two higher rate excursions in the data and two compaction bands in the recovered sample. The association between such excursions and the growth of compaction bands is further supported by the AE location data of Figure 9, in which we see a broad localized band form during a large excursion (see strain interval (e) in Figure 9d). From these data and observations we can conclude that, whereas compaction band formation during constant strain rate experiments is coincident with small stress drops (see *Baud et al*., 2004), their formation is associated with positive excursions in the axial strain rate (and concomitant positive excursions in AE energy rate and porosity reduction rate) during compaction creep.

If we assume that each excursion represents the growth of a compaction band, then we can estimate the inelastic strain accumulated during the growth of each compaction band in our compaction creep experiments by simply measuring the amount of axial strain during a particular excursion (assuming that all strain accumulated after C* is inelastic). The data, for each observable excursion, are plotted against the background strain rate (the characteristic creep strain rate prior to and following the excursion) in Figure 13a. The data of Figure 13a show that the inelastic strain associated with the growth of the compaction bands observed in this study changes relatively little even as the baseline strain rate varies over three orders of magnitude (from 10^{-5} to 10^{-8} s^{-1}). In other words, this suggests that the inelastic strain associated with the growth of a compaction band does not depend on the level of applied stress or the baseline strain rate. In addition, the duration of any particular excursion allows us to estimate the band growth rate, assuming that the band traverses the full diameter of the sample (20 mm). Compaction band growth rates (for all of the excursions included in Figure 13a) are plotted against their background strain rate in Figure 13b. We observe that the growth rate of the compaction bands is very much dependent on the baseline strain rate; in

fact, the slope of the curve is essentially one. Individual compaction band growth durations vary from several minutes to several days, corresponding to growth rates between about 10^{-4} and about 10^{-7} m s^{-1} (Figure 13b). Therefore, the inelastic strain associated with the growth of a compaction band does not depend on either the growth duration or the growth rate. This suggests that the formation of a compaction band corresponds to the fracture of a plane of grains typically two or three grains thick, independently of the time required. The scatter in the strain and growth rate data of Figure 13 can be explained, at least in part, by the variation in the geometrical attributes of the bands, for example the growth of multiple, partial or branched bands rather than just discrete, single bands. The SEM photomicrographs of Figures 12 and 14 illustrate some of this geometrical complexity, showing partial bands (Figure 14a), bands containing multiple strands (Figure 14b) and discrete bands (Figure 12c).

4.2 Comparisons of compaction band characteristics between constant strain rate and constant stress conditions

To assess any differences between compaction bands grown under constant stress and constant strain rate conditions, we first estimated the inelastic strain associated with the growth of compaction bands under a constant strain rate, to compare with the data shown in Figure 13a for constant stress conditions. Here, and following *Baud et al*. (2004), we associate the growth of compaction bands under a constant strain rate with a stress drop and an excursion in the rate of AE activity. We find that the inelastic strain associated with the growth of a compaction band is about the same (between 0.1 and 0.5%) regardless of whether the band grew under a constant stress or a constant strain rate (Figure 13a). We note that the inelastic strain associated with the growth of a compaction band in Bentheim sandstone under a constant strain rate of 10^{-5} s^{-1} also falls within this range (0.4%; *Baud et al*., 2004). We also calculated the compaction band growth rates for the bands formed during our constant strain

rate experiments, using the measured inelastic strain and the imposed strain rate (again assuming that the bands traverse the full diameter of the sample). The results are plotted (as open circles) alongside the growth rates for the bands formed during compaction creep in Figure 13b. We find that compaction band growth rates under constant strain rate conditions are entirely consistent with the general trend for band growth rate in the constant stress creep experiments. Further, the rates of band growth during our constant strain rate experiments are very similar to the rate determined for compaction band growth in Diemelstadt sandstone (8×10^{-5} m s^{-1}) by *Townend et al*. (2008). The experiment of *Townend et al*. (2008), also performed at a constant strain rate of 10^{-5} s^{-1}, further strengthens the observed relationship between background strain rate and the band growth rate shown in Figure 13b.

A comparison of the P-wave velocity evolution with strain between a constant strain rate and a constant stress experiment conducted under the same effective stress in the compactant regime (Peff = 80 MPa) is presented as Figure 15. If we compare the P-wave speeds for one direction, 90° to the compression axis, the P-wave speed during the constant strain rate experiment (grey curve) steadily decreases with increasing inelastic strain, resulting in an overall decrease of about 9% at a strain of 5%, while during the creep experiment (blue curve) the speed decreases in the same manner, with a decrease of about 7% after 4.5% strain. These steady reductions in P-wave speed imply the progressive nucleation and growth of microcracks (see also *Ayling et al*., 1995). Furthermore, the observation that the decrease in P-wave speed is a maximum in the radial direction and progressively decreases at lower angles to the sample axis is compatible with the development of a P-wave anisotropy with the preferential growth of axial microcracks, as observed previously during cataclastic flow in sandstone (*Wu et al*., 2000).

Overall, the data therefore suggest that the microstructural evolution during compaction creep is essentially the same between the two experimental regimes, regardless of

the very large differences in strain rates and compaction band growth rates (as shown in Figure 13). Hence, as indicated earlier, we find no discernible difference between the microstructural characteristics of the compaction bands formed under the different experimental conditions (Figure 12). Our assessment leads to the conclusion that the characteristics of compaction bands are essentially identical however they are formed.

4.3 Stress dependency and creep compaction rates

Since the inelastic strain required to grow a compaction band is essentially constant over a wide range of strain rates (Figure 13a), an understanding of the stress dependency of compaction creep rates will allow us to estimate the time required to grow compaction bands at strain rates impracticable to achieve over typical laboratory timescales (i.e., experiment durations from months to years).

It is important to first note that our compaction creep experiments show that the differential stress required for the onset of compaction band formation is significantly lower than that required during constant strain rate experiments. For example the constant strain rate experiment reported in Figure 4 showed that compaction bands development started at a differential stress of about 100 MPa (for Peff = 80 MPa). By contrast, our compaction creep experiments suggest that compaction bands can develop at differential stresses as low as 80 MPa (Figure 8). We hypothesize that, given sufficient time, compaction bands could grow at any stress above that required for the onset of inelastic compaction (C*; about 45 MPa at a Peff of 80 MPa, see Figure 2). Below C* the rock is assumed to be poroelastic and should therefore not accumulate damage under constant stress. Following a similar argument, it was previously postulated that shear fracture formation during dilatant creep could only occur above the stress level required for the onset of microcracking (C'; *Heap et al.*, 2009a). Our stress-stepping creep test has shown that a 10 MPa increase in differential stress increased the

creep strain rate by approximately two orders of magnitude (Figure 11). A crude extrapolation of the computed compaction creep strain rates from Figure 11 to lower values of stress suggest that a strain rate of the order of 10^{-12} s^{-1} may be reached at a differential stress of about 70 MPa. At 45 MPa (the position of C* at Peff = 80 MPa), the hypothesized lower limit for compaction creep under these conditions, the extrapolated strain rate reaches an astonishingly low value of 10^{-16} s^{-1}, significantly lower than the background tectonic strain rate of the crust. However, since this is our projected lower limit for shear-enhanced compaction under a constant stress, the suggestion that the deformation essentially stops at this stress level is entirely as predicted.

A more detailed analysis of the stress dependency of compaction creep is presented in Figure 16. Firstly, Figure 16a shows an evaluation of the stress dependency of the creep strain rate using our conventional creep experiments (Q = 60, 70, 80, 85, 90, and 97.5 MPa; Peff = 80 MPa). The data show that the creep strain rate, measured in each test at the same inelastic strain of 2.39%, increases by four orders of magnitude from about 10^{-9} to 10^{-5} s^{-1} as differential stress is increased by 35 MPa from 60 to 95 MPa; similar to the increases observed in the stress-stepping experiment (Figure 11). Following the method of *Brantut et al*. (2014a), we can also investigate how the creep strain rate in a single creep experiment evolves as a function of the stress difference between the creep test and a constant strain rate test performed under the same effective pressure. Such an analysis is only valid if the microstructural state of the samples, deforming under different stresses and strain rates, can be considered to be a simple function of the level of inelastic axial strain. In the present study, as was the case for *Brantut et al*. (2014a), this assumption is strongly supported by the observation that the evolution of P-wave speed with inelastic strain between the two types of experiment is essentially the same (Figure 15). The strain rates for the two creep tests performed at the two lowest creep stresses (Q = 60 MPa and Q = 70 MPa) are plotted as a

function of the stress difference (ΔQ) between the constant stress applied during the creep test and the differential stress acting on a sample deforming under a constant strain rate at the same inelastic strain (Figure 16b). We find that the evolution of strain rate with the stress difference is very similar for the two experiments. Whereas this type of analysis yields two branches in the dilatant regime corresponding to the initial decrease in strain rate during primary creep and the subsequent increase in strain rate associated with tertiary creep, respectively (*Brantut et al*., 2014a), here we observe only one branch in the compactant regime owing to the fact that the axial strain rate decreases continuously throughout creep compaction (Figure 16b). The similarity in slopes between the data from multiple individual creep tests plotted in Figure 16a, and the data calculated from two creep tests in Figure 16b using the method of *Brantut et al*. (2014a) suggest that the stress difference method is a viable and valid method for determining the stress dependence of creep compaction. The slope of these curves has been interpreted in terms of an "activation" stress σ* that provides the stress dependency of the creep strain rate, where $\dot{\varepsilon}_{creep}/\dot{\varepsilon}_0 \approx \exp(\Delta Q/\sigma^*)$ (*Brantut et al*., 2014a). Where $\dot{\varepsilon}_{creep}$ is the instantaneous brittle creep strain rate and $\dot{\varepsilon}_0$ is the strain rate applied during the constant strain rate test (equal to 10^{-5} s^{-1}). We calculate σ* values of 4.0 and 5.8 MPa for the experiments at creep stresses of 60 and 70 MPa, respectively (Figure 16b). However, there are limitations to this method. Figure 17 shows the strain rate as a function of the stress difference for a compaction creep experiment performed at a higher creep stress (Q = 80 MPa), plotted alongside those data from Figure 16b. We notice that, although the data from the Q = 80 MPa test follow the trend of the two other tests at low stress difference values, the axial strain rate is reduced without any further reduction in the stress difference at a stress difference of about 20 MPa. This phenomenon is a result of the stress-strain curve of the constant strain rate experiment reaching a stress plateau (see Figure 5b), coupled with the fact that the strain rate during creep compaction continues to decrease

(e.g., Figure 6b). While a similar interpretation of the slope of the Q = 80 MPa test would yield two values for σ*, one similar to that of the other two experiments and one considerably higher, we highlight that the empirical micromechanical model of *Brantut et al*. (2014a) requires an effective crack length and an average fracture toughness, assumptions that are not respected when the strain is localized. We can conclude that, in terms of the model, the slope defined by the reduction in creep strain rate at an almost constant stress difference is likely meaningless due to the appearance of strain localization at inelastic strains comparable with the stress plateau in a constant strain rate experiment; compaction band formation was not observed in the two experiments at low creep stresses (Q = 60 MPa and Q = 70 MPa). Therefore, in the analysis of the stress dependency of the creep compaction, care is needed to avoid the analysis of data at inelastic strains likely to involve strain localization (i.e., the formation of compaction bands).

4.4 Microstructural creep compaction mechanism

Time-dependent damage accumulation in the dilatant regime, leading to shear fracture formation, has been previously explained in terms of stress corrosion cracking (e.g., *Kranz et al*., 1982; *Ngwenya et al*., 2001; *Heap et al.*, 2009a; *Brantut et al.*, 2013). Stress corrosion cracking is therefore also a prime candidate for the microstructural mechanism responsible for the formation of time-dependent compaction bands. Several lines of experimental and microstructural evidence support this hypothesis. Firstly, the evolution of the AE energy during compaction creep closely follows that of the axial strain (Figure 6b), as it also does during dilatant creep (Figure 6a). This suggests that microcracking (contact or Hertzian cracking leading to the crushing of grains; see *Zhang et al*., 1990) is the process responsible for the deformation. Indeed, our microstructural observations show that the occurrence of compaction bands in sandstone is the result of intensive microcracking and grain

comminution (Figure 12); as also shown in previous studies of compaction band formation in sandstones (e.g., *Baud et al*., 2004; *Fortin et al*., 2006). Microcracking as the mechanism responsible for the observed time-dependent deformation is also supported by our AE location analysis (Figure 9d) and the decrease in P-wave velocity with strain during both constant strain rate and constant stress experiments (Figure 15). Time-dependent microcracking is more consistent with a stress corrosion cracking mechanism, rather than other time-dependent processes such as pressure-solution (e.g., *Rutter and Elliot*, 1976), or the visco-elastic behaviour observed, for example, during the time-dependent deformation of shale (*Sone and Zoback*, 2014). Pressure-solution would, for instance, likely result in a difference in P-wave velocity evolution with increasing inelastic strain at different strain rates, as reported for porous limestone (*Brantut et al*., 2014b). We note that no evidence of any pressure-solution features were found during the microstructural analysis of our deformed samples (Figure 12), and that pressure solution is highly unlikely to be responsible for the observed AE activity during our creep compaction experiments.

Perhaps most pertinently, the stress dependence of the creep strain rate in the compactant regime (Figure 16a) appears to follow a very similar form as the stress dependence of creep in the dilatant regime (e.g., *Brantut et al.*, 2014a). In general, in both regimes, an increase in differential stress of about 5 MPa leads to an increase in creep strain rate of about an order of magnitude. To investigate further the similarity of the stress dependence of creep in the compactant and dilatant regimes, we computed the strain rate as a function of stress difference for our creep experiment performed in the dilatant regime; and the decelerating branch of these data are plotted alongside the compaction creep data of Figure 16b in Figure 18. We find the activation stress σ^* in the dilatant regime to be 1.0 MPa, a value similar to that for other porous sandstones in the dilatant regime (at effective pressures from 10 to 40 MPa; *Brantut et al*., 2014a). Although the activation stress during

compaction creep is higher by a factor of about 5, we contend that this difference is likely due to differences in microscale parameters (such as crack geometry, crack interactions) between creep in the dilatant and compaction regimes, rather than a change in the responsible micromechanical mechanism. For example, the onset of grain crushing at C*, unlike the onset of dilatational microcracking at C', does not require that frictional forces are overcome before the initiation of cracking. Grain crushing is solely a function of the fracture toughness of the material and the contact stresses between grains (*Zhang et al*., 1990). Further, the micromechanical approach of *Brantut et al*. (2014a) assumes that the relation between the differential stress and the average stress intensity factor does not change with confining pressure and, while this assumption is valid over the range of effective pressures associated with the dilatant regime, it may not retain validity at the higher effective pressures associated with the compactant regime. Therefore, although the cracks may be growing by the mechanism of stress corrosion cracking in both regimes, differences in the macroscopic features—shear fracture in the dilatant regime and compaction bands in the compactant regime—are interpreted as resulting from differences in crack geometries and interaction processes under different effective pressures.

We conclude that environment-dependent stress corrosion cracking facilitates time-dependent deformation in both the dilatant and compactant regimes. It is therefore likely that compaction creep will be greatly influenced by temperature (e.g., *Meredith and Atkinson*, 1982; *Kranz et al*., 1982; *Heap et al*., 2009b) and the chemistry of the pore fluid (*Atkinson and Meredith*, 1981).

4.5 Time-dependent porosity loss, subsidence, and permeability reduction in sandstone reservoirs

Time-dependent compaction, and the formation of time-dependent compaction bands, is likely an important crustal deformation process in porous rocks. For example, the differential stress required for the onset of grain crushing at C* is reduced at higher effective pressures or greater depths (*Wong and Baud*, 2012). Therefore, if the minimum stress required to allow compaction creep and the development of compaction bands is given by C* (see above discussion), then time-dependent compaction will be able to initiate at lower differential stresses as depth in the crust increases. We therefore outline below some implications of time-dependent compaction for deformation of sandstone reservoirs.

Production-induced reservoir compaction can result in subsidence and is therefore an important consideration in reservoir management and the optimization and productivity of reservoirs. For instance, subsidence can require the expensive redesign of offshore platforms, and lead to an enhanced risk of pipeline and casing damage, induced-seismicity, and even the flooding of offshore platforms (e.g., *Nagel*, 2001; *Schutjens et al*., 2004 and references therein). Our study has demonstrated that time-dependent mechanical porosity loss in sandstone reservoirs, promoting time-dependent subsidence and reservoir quality reduction, may emerge as an important consideration in reservoir management, especially following intervals of hydrocarbon production and groundwater extraction (e.g., *Hettema et al*., 2000; *Schutjens et al*., 2004); although we recognize that other contributing processes, such as pressure solution and cementation, may also play an important role under certain conditions of stress and temperature (e.g., *Houseknecht*, 1987; *Dewers and Hajash*, 1995; *Walderhaug*, 1996). However, while porosity loss due to mechanical compaction is generally considered subsidiary to high-temperature quartz cementation deeper in reservoirs (*Ajdukiewicz and Lander*, 2010), we highlight that stress corrosion cracking in quartz (*Meredith and Atkinson*,

1982) and sandstones (*Heap et al*., 2009b) is highly temperature-dependent. For example, the strain rate during a constant stress experiment can be increased by multiple orders of magnitude upon increasing the temperature by as little as 50 °C (*Heap et al*., 2009b). Mechanical compaction, assisted by environment-dependent stress corrosion cracking, could therefore play a significant role in porosity reduction within deep sandstone reservoirs.

Our study has also shown that compaction localization in sandstone—compaction band formation—is time-dependent. Therefore, in sandstone reservoirs with a well-sorted grain size distribution, compaction bands can develop gradually (at a rate dependent on the magnitude of the prevalent stress) but then suddenly and severely impact permeability (e.g., *Baud et al*., 2012; *Deng et al*., 2015; *Ballas et al*., 2015). Flow simulation modelling has suggested that the presence of compaction bands can exert a profound influence on subsurface flow at scales relevant to aquifer and reservoir production (*Sternlof et al*., 2006). In detail, the modelling of *Sternlof et al*. (2006) shows that the presence of compaction bands can result in a three-fold increase in the pressure drop required to maintain a given flow rate between two wells, and a pronounced tendency for fluids to flow parallel to the dominant band orientation regardless of the regional hydraulic gradient. We anticipate that a detailed understanding of time-dependent compaction and compaction band formation in reservoirs is essential for the continued utilization and management (using reservoir quality predictive models) of a particular field.

5. Concluding remarks and perspective

The constant stress experiments of this study reveal that strain can accumulate at constant stress in the compactant regime, and that this strain accumulation can result in the growth of compaction bands. In detail, creep compaction (deformation at a constant stress) is characterized by decelerating rates of axial strain, acoustic emission energy, and porosity

reduction. The formation of compaction bands during compaction creep is thought to occur during the higher rate excursions that punctuate this global decelerating trend. We show that compaction bands can develop at stresses much lower than previously considered, and speculate that creep compaction, and the growth of time-dependent compaction bands, can occur at any stress above that required for the onset of shear-enhanced compaction. This suggests that, in support of previous studies (e.g., *Wong and Baud*, 2012), the onset of shear-enhanced compaction represents the most logical position to test theoretical predictions of localization based on bifurcation analysis (e.g., *Rudnicki and Rice*, 1975; *Issen and Rudnicki*, 2000).

We find that the rate of creep compaction is highly dependent on the applied differential stress (an increase in the differential stress of about 10 MPa increases the rate of creep compaction by about two orders of magnitude). As a result, the growth rate of compaction bands is highly dependent on the background strain rate and hence the applied differential stress; indeed, the growth rate of compaction bands can be orders of magnitude slower than those formed at the strain rate typically used in laboratory constant strain rate experiments (10^{-5} s^{-1}). However, despite the order of magnitude differences in strain rate and band growth rate between the constant stress and constant strain rate experiments, the inelastic strain associated with the growth of a compaction band and the characteristics (geometry, thickness) of the compaction bands remain essentially constant. Several lines of evidence, notably the similar stress dependence of the creep strain rate in the compactant and dilatant regimes, suggest that stress corrosion cracking is the main mechanism responsible for creep compaction and the development of compaction bands under a constant stress. Stress corrosion is likely therefore an important deformation mechanism in both the upper and lower crust.

Time-dependent compaction and compaction localization is likely to play a key role in the evolution of sandstone reservoirs. Creep compaction will reduce porosity over time, leading to a reduction in reservoir quality and the problems associated with subsidence. Further, slow-growing compaction bands can encourage reservoir compartmentalization and severely reduce permeability, thus channeling flow and affecting the pressure drop required to maintain a flow rate between wells. A detailed understanding of time-dependent compaction and compaction band formation in reservoirs is therefore essential for the continued reservoir utilization and management.

Acknowledgements

The authors are extremely grateful to Neil Hughes, John Bowles, Steve Boon, and Thierry Reuschlé for experimental assistance and support. We also acknowledge Peter Sammonds for his role in the design and development of the 400 MPa triaxial press and jacketing system at UCL. Nicolas Brantut and Philip Meredith were partly funded by UK NERC grant NE/G016909/1 "Time-dependent deformation: bridging the strain rate gap in brittle rocks". Nicolas Brantut also acknowledges support from NERC grant NE/K009656/1. Patrick Baud and Michael Heap were partly funded by the CNRS under the PICS grant 5993. We thank Alexandra Kushnir for the permeability datum, and Philip Benson for loan of his acoustic emission recording system for the experiments performed at UCL. The original data used in producing this paper can be made available upon request.

References

Anderson, O.L., and Grew, P.C. (1977), Stress Corrosion Theory of Crack Propagation with Applications to Geophysics, *Reviews of Geophysics*, *15*, 77-104.

Ajdukiewicz, J.M., and Lander, R.H. (2010), Sandstone reservoir quality prediction: The state of the art, *AAPG Bulletin*, *94*, 1083-1091.

Atkinson, B.K., and Meredith, P.G. (1981), Stress corrosion cracking of quartz: A note on the influence of chemical environment, *Tectonophysics*, *77*, 1-11.

Atkinson, B.K. (1982), Subcritical crack propagation in rock: theory, experimental results and applications, *Journal of Structural Geology*, *4*, 41-56.

Atkinson, B. K. (1984), Subcritical crack growth in geological materials, *Journal of Geophysical Research*, *89*, 4077-4114.

Atkinson, B.K., and Meredith, P.G., 1987, The theory of subcritical crack growth with applications to minerals and rocks, *in* Atkinson, B.K., ed., Fracture Mechanics of Rock: London, Academic Press, p. 111-166.

Aydin, A., and Ahmadov, R. (2009), Bed-parallel compaction bands in aeolian sandstone: Their identification, characterization and implications, *Tectonophysics*, *479*, 277-284.

Ayling, M.R., Meredith, P.G., and Murrell, S.A.F. (1995), Microcracking during triaxial deformation of porous rocks monitored by changes in rock physical properties, I. Elastic-wave propagation measurements on dry rocks, *Tectonophysics*, *245*, 205-221.

Ballas, G., Soliva, R., Sizun, J.-P., Fossen, H., Benedicto, A., and Skurtveit, E. (2013), Shear-enhanced compaction bands formed at shallow burial conditions; implications for fluid flow (Provence, France), *Journal of Structural Geology*, *47*, 3-15.

Ballas, G., Fossen, H., and Soliva, R. (2015), Factors controlling permeability of cataclastic deformation bands and faults in porous sandstone reservoirs, *Journal of Structural Geology*, *76*, 1-21.

Baud, P., E. Klein, and T.-f. Wong (2004), Compaction localization in porous sandstones: spatial evolution of damage and acoustic emission activity, *Journal of Structural Geology*, *26*, 603-624.

Baud, P., E. Townend, and P. G. Meredith (2012), Permeability evolution during triaxial compaction of an anisotropic porous sandstone, *Journal of Geophysical Research*, doi: 10.1029/2012JB009176.

Borja, R.I., and Aydin, A. (2004), Computational modeling of deformation bands in granular media. I. Geological and mathematical framework, *Comput. Methods Appl. Mech. Engrg.*, *193*, 2667-2698.

Brantut, N., M. J. Heap, P. G. Meredith, and P. Baud (2013), Time-dependent cracking and brittle creep in crustal rocks: A review, *Journal of Structural Geology*, *52*, 17-43.

Brantut, N., M. J. Heap, P. Baud, and P. G. Meredith (2014a), Rate- and strain-dependent brittle deformation of rocks, *Journal of Geophysical Research, 119,* 1818-1836.

Brantut, N., M. J. Heap, P. Baud, and P. G. Meredith (2014b), Mechanisms of time-dependent deformation in porous limestone, *Journal of Geophysical Research, 119*(7), 5444-5463.

Brzesowsky, R.H., Hangx, S.J.T., Brantut, N., and Spiers, C.J. (2014), Compaction creep of sands due to time-dependent grain failure: effects of chemical environment, applied stress and grain size *Journal of Geophysical Research, 119,* DOI:10.1002/2014JB011277.

Charalampidou, E.-M.H., S. A., Stanchits, S., Lewis, H., and Viggiani, G. (2011), Characterization of shear and compaction bands in a porous sandstone deformed under triaxial compression, *Tectonophysics, 503,* 8-17.

Chester, J.S., Lenz, S.C., Chester, F.M., and Lang, R.A. (2004), Mechanisms of compaction of quartz sand at diagenetic conditions, *Earth and Planetary Science Letters, 220,* 435-451.

Cheung, C., P. Baud, and T.-f. Wong (2012), Effect of grain size distribution on the development of compaction localization in porous sandstone, *Geophysical Research Letters, 39*(21), DOI: 10.1029/2012GL053739.

Costin, 1987, Time-dependent deformation and failure, *in* Atkinson, B.K., ed., Fracture Mechanics of Rock: London, Academic Press, p. 167–216.

David, C., Menéndez, B., Zhu, W., and Wong, T.-f. (2001), Mechanical compaction, microstructures and permeability evolution in sandstones, *Physics and Chemistry of the Earth, 26,* 45-51.

Deng, S., Zuo, L., Aydin, A., Dvorkin, J., and Mukerji, T. (2015), Permeability characterization of natural compaction bands using core flooding experiments and three-dimensional image-based analysis: Comparing and contrasting the results from two different methods, *AAPG Bulletin, 99,* 27-49.

Dewers, T., and Hajash, A. (1995), Rate laws for water-assisted compaction and stress-induced water-rock interaction in sandstones, *Journal of Geophysical Research, 100 (B7),* 13093-13112.

Eccles, D., Sammonds, P.R., and Clint, O.C. (2005), Laboratory studies of electrical potential during rock failure *International Journal of Rock Mechanics and Mining Sciences, 42,* 933-949.

Eichhubl, P., Hooker, J.N., and Laubach, S.E. (2010), Pure and shear-enhanced compaction bands in Aztec Sandstone, *Journal of Structural Geology, 32,* 1873-1886.

Fortin, J., Stantchits, S., Dresen, G., and Guéguen, Y. (2006), Acoustic emission and velocities associated with the formation of compaction bands in sandstone, *Journal of Geophysical Research, 111 (B10),* DOI: 10.1029/2005JB003854.

Fujii, Y., Kiyama, T., Ishijima, Y., and Kodama, J. (1999), Circumferential strain behavior during creep tests of brittle rocks, *International Journal of Rock Mechanics and Mining Sciences*, *36*, 323-337.

He, W., Hajash, A., and Sparks, D. (2003), Creep compaction of quartz aggregates: Effects of pore-fluid flow—A combined experimental and theoretical study, *American Journal of Science*, *303*, 73-93.

Heap, M. J., P. Baud, P. G. Meredith, A. F. Bell, and I. G. Main (2009a), Time-dependent brittle creep in Darley Dale sandstone, *Journal of Geophysical Research*, *114*, *B07203*, doi: 10.1029/2008JB006212.

Heap, M.J., Baud, P., and Meredith, P.G. (2009b), The influence of temperature on brittle creep in sandstones, *Geophysical Research Letters*, *36*, *L19305*, DOI: 10.1029/2009GL039373.

Heap, M. J., P. Baud, P. G. Meredith, S. Vinciguerra, A. F. Bell, and I. G. Main (2011), Brittle creep in basalt and its application to time-dependent volcano deformation, *Earth and Planetary Science Letters*, *307*, 71-82.

Hettema, M.H.H., Schutjens, P.M.T.M., Verboom, B.J.M., and Gussinklo, H.J. (2000), Production-Induced Compaction of a Sandstone Reservoir: The Strong Influence of Stress Path, *SPE Reservoir Evaluation & Engineering, Society of Petroleum Engineers*, *3 (SPE-65410-PA)*, DOI: http://dx.doi.org/10.2118/65410-PA.

Hill, R.E. (1989), Analysis of Deformation Bands in the Aztec Sandstone, Valley of Fire State Park, Nevada, *M. S. thesis, University of Nevada, Las Vegas*, pp. 68.

Holcomb, D.J., and Olsson, W.A. (2003), Compaction localization and fluid flow, *Journal of Geophysical Research*, *108*, B6, DOI: 10.1029/2001JB000813.

Houseknecht, D.W. (1987), Assessing the Relative Importance of Compaction Processes and Cementation to Reduction of Porosity in Sandstones, *AAPG Bulletin*, *71*, 633-642.

Ingraham, M.D., Issen, K.A., and Holcomb, D.J. (2013), Response of Castlegate sandstone to true triaxial states of stress, *Journal of Geophysical Research*, *118*, 536-552.

Issen, K.A., and Rudnicki, J.W. (2000), Conditions for compaction bands in porous rock, *Journal of Geophysical Research*, *105*, 21529-21536.

Karner, S.L., Chester, F.M., Kronenberg, A.K., and Chester, J.S. (2003), Subcritical compaction and yielding of granular quartz sand, *Tectonophysics*, *377*, 357-381.

Katsman, R., Aharonov, E., and Scher, H. (2005), Numerical simulation of compaction bands in high-porosity sedimentary rock, *Mechanics of Materials*, *37*, 143-162.

Kranz, R., Harris, W.J., and Carter, N.L. (1982), Static fatigue of granite at 200 °C, *Geophysical Research Letters*, *9*, 1-4.

Le Guen, Y., Renard, F., Hellmann, R., Brosse, E., Collombet, M., Tisserand, D., and Gratier, J.-P. (2007), Enhanced deformation of limestone and sandstone in the presence of high PCO2 fluids, *Journal of Geophysical Research, 112 (B05421)*, DOI: 10.1029/2006JB004637.

Lockner, D., Byerlee, J., Kuksenko, V., Ponomarev, A., and Sidorin, A. (1991), Quasi-static fault growth and shear fracture energy in granite, *Nature, 350*, 39-42.

Louis, L., Wong, T.-f., and Baud, P. (2007), Imaging strain localization by X-ray radiography and digital image correlation: Deformation bands in Rothbach sandstone, *Journal of Structural Geology*, *29*, 129-140.

Meredith, P.G., and Atkinson, B.K. (1982), High-temperature tensile crack propagation in quartz: Experimental results and application to time-dependent earthquake rupture, *Earthquake Predict. Res.*, *1*, 377-391.

Mollema, P.N., and Antonellini, M.A. (1996), Compaction bands: a structural analog for anti-mode I cracks in aeolian sandstone, *Tectonophysics*, *267*, 209-228.

Nagel, N.B. (2001), Compaction and subsidence issues within the petroleum industry: From wilmington to ekofisk and beyond, *Physics and Chemistry of the Earth, Part A: Solid Earth and Geodesy*, *26*, 3-14.

Ngwenya, B.T., Main, I.G., Elphick, S.C., Crawford, B.R., and Smart, B.G.D. (2001), A constitutive law for low-temperature creep of water-saturated sandstones, *Journal of Geophysical Research, 106*, 21811-21826.

Rudnicki, J.W., and Rice, J.R. (1975), Conditions for the localisation of deformation in pressure-sensitive dilatant materials, *J. Mech. Phys. Solids*, *23*, 371-394.

Rutter, E., and Elliot, D. (1976), The Kinetics of Rock Deformation by Pressure Solution [and Discussion], *Phil. Trans. Royal Soc. London*, DOI: 10.1098/rsta.1976.0079.

Schultz, R.A., Okubo, C.H., and Fossen, H. (2010), Porosity and grain size controls on compaction band formation in Jurassic Navajo Sandstone, *Geophysical Research Letters*, *37 (L22306)*, DOI:10.1029/2010GL044909.

Schutjens, P.M.T.M., Hanssen, T.H., Hettema, M.H.H., de Bree, P., Coremans, J.W.A., and Helliesen, G. (2004), Compaction-Induced Porosity/Permeability Reduction in Sandstone Reservoirs: Data and Model for Elasticity Dominated Deformation, *SPE Reservoir Evaluation & Engineering, Society of Petroleum Engineers, 7 (SPE-88441-PA)*, DOI: http://dx.doi.org/10.2118/88441-PA.

Sone, H., and Zoback, M.D. (2014), Time-dependent deformation of shale gas reservoir rocks and its long-term effect on the in situ state of stress, *International Journal of Rock Mechanics and Mining Sciences*, *69*, 120-132.

Sternlof, K.R., Rudnicki, J.W., and Polland, D.D. (2005), Anticrack inclusion model for compaction bands in sandstone, *Journal of Geophysical Research, 110 (B11)*, DOI: 10.1029/2005JB003764.

Sternlof, K.R., Karimi-Fard, M., Polland, D.D., and Durlofsky, L.J. (2006), Flow and transport effects of compaction bands in sandstone at scales relevant to aquifer and reservoir management, *Water Resources Research, 42*, DOI: 10.1029/2005WR004664.

Tembe, S., Baud, P., and Wong, T.-F. (2008), Stress conditions for the propagation of discrete compaction bands in porous sandstone, *Journal of Geophysical Research, 113 (B9)*, DOI: 10.1029/2007JB005439.

Thomsen, L. (1986), Weak elastic anisotropy, *Geophysics*, *51*, 1954-1966.

Townend, E., Thompson, B.D., Benson, P.M., Meredith, P.G., Baud, P., and Young, R.P. (2008), Imaging compaction band propagation in Diemelstadt sandstone using acoustic emission locations, *Geophysical Research Letters, 35 (L15301)*, DOI: 10.1029/2008GL034723.

Walderhaug, O. (1996), Kinetic Modeling of Quartz Cementation and Porosity Loss in Deeply Buried Sandstone Reservoirs, *AAPG Bulletin, 80*, 731-745.

Wang, B., Y. Chen, and T.-f. Wong (2008), A discrete element model for the development of compaction localization in granular rock, *Journal of Geophysical Research, 113*, B03202, doi:03210.01029/02006JB004501.

Wong, T.-f., and P. Baud (2012), The brittle-ductile transition in rocks: a review, *Journal of Structural Geology, 44*, 25-53.

Wong, T.-f., C. David, and W. Zhu (1997), The transition from brittle faulting to cataclastic flow in porous sandstones: Mechanical deformation, *Journal of Geophysical Research, 102*(No. B2), 3009-3025.

Wu, X.Y., Baud, P., and Wong, T.-F. (2000), Micromechanics of compressive failure and spatial evolution of anisotropic damage in Darley Dale sandstone, *International Journal of Rock Mechanics and Mining Sciences, 37*, 143-160.

Yang, S., and Jiang, Y. (2010), Triaxial mechanical creep behavior of sandstone, *Mining Science and Technology, 20*, 339-349.

Zhang, J., Wong, T.-F., and Davis, D.M. (1990), Micromechanics of Pressure-Induced Grain Crushing in Porous Rocks, *Journal of Geophysical Research, 95, No. B1*, 341-352.

Zhu, W., and Wong, T.-f. (1997), The transition from brittle faulting to cataclastic flow: Permeability evolution, *Journal of Geophysical Research, 102, No. B2*, 3027-3041.

Table 1

Experimental summary of the 12 experiments presented in this study. Experiments on samples bvs-03 and bvs-04 were performed at University College London; the remainder were performed at the Université de Strasbourg.

Sample	Connected porosity	Effective pressure (MPa)	Pore pressure (MPa)	Strain rate (s^{-1})	Creep stress (MPa)	Creep duration (minutes)	Peak stress (MPa)	C* (MPa)	Notes
bws16	0.245	10	10	10^{-5}	-	-	74	-	
bws11	0.245	80	10	10^{-5}	-	-	-	-	Taken to 13% strain
bws21	0.245	80	10	10^{-5}	-	-	-	-	Taken to 1.5% strain
bws22	0.246	80	10	10^{-5}	-	-	-	-	Taken to 3% strain
bvs-04	0.236	80	10	10^{-5}	-	-	-	-	AE locations and P-wave speeds
bws17	0.245	10	10	-	63	820	63	-	
bws4	0.242	80	10	-	60	4035	-	46.6	
bws5	0.240	80	10	-	70	3958	-	47.7	
bws6	0.245	80	10	-	80	7164	-	44.7	
bws3	0.245	80	10	-	90	1458	-	47.2	
bws7	0.238	80	10	-	85-100	-	-	45.8	Stress-stepping creep test
bvs-03	0.239	80	10	-	92.2	4310	-	44.3	AE locations and P-wave speeds

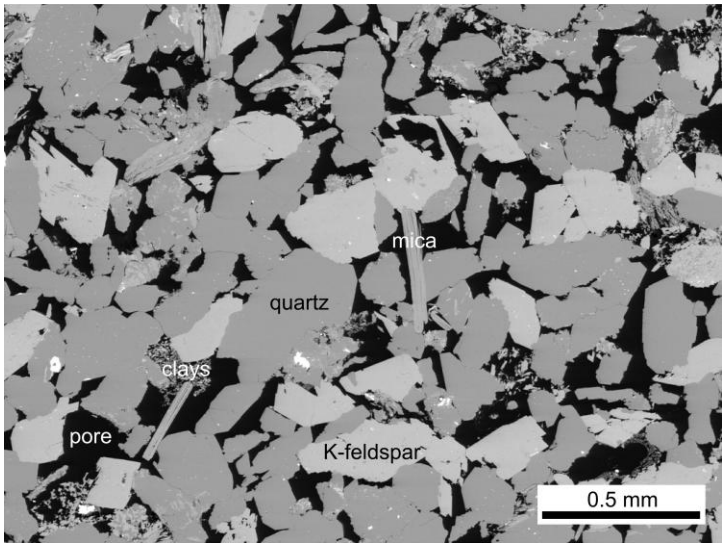

Figure 1. Back scattered electron photomicrograph of Bleurswiller sandstone (Bleurville, Vosges, north-eastern France). The main mineralogical components, and a pore, are labelled on the picture.

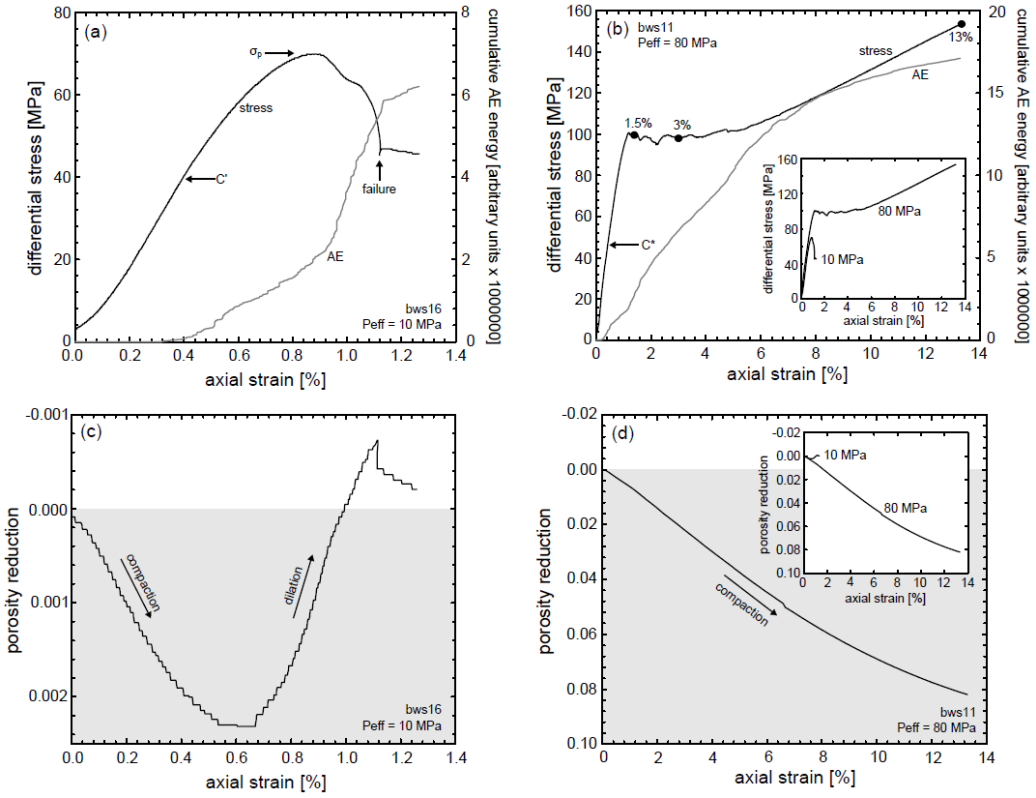

Figure 2. Bleurswiller sandstone constant strain rate experiments. (a) Differential stress and accumulative acoustic emission energy as a function of axial strain for a sample deformed in the dilatant regime (effective pressure = 10 MPa). The onset of dilatational microcracking C', the peak stress σ_p, and the position of sample failure are indicated on the stress-strain curve. (b) Differential stress and accumulative acoustic emission energy as a function of axial strain for a sample deformed in the compactant regime (effective pressure = 80 MPa). The onset of shear-enhanced compaction C* is indicated on the stress-strain curve. Inset shows the stress-strain curves of panels (a) and (b) plotted on axes of the same scale. Black circles correspond to the positions at which deformation was arrested in three experiments for macroscopic sample observations (see Figure 3) and microstructure (see Figure 12). (c) The porosity reduction curve for the dilatant experiment shown in panel (a). The grey zone denotes the area of net compaction. (d) The porosity reduction curve for the compactant experiment shown in panel (b). The grey zone denotes the area of net compaction. Inset shows the porosity reduction curves of panels (c) and (d) plotted on axes of the same scale.

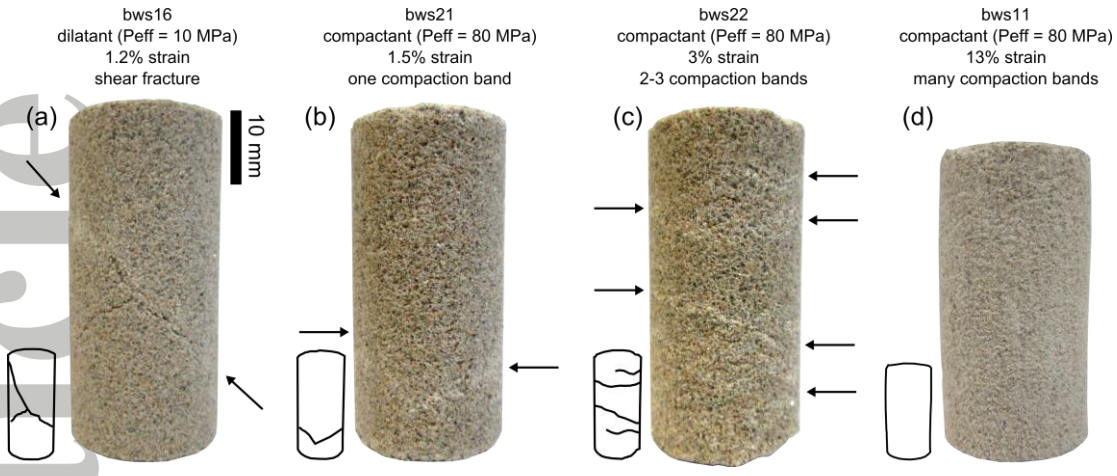

Figure 3. Failure modes. Photographs of samples of Bleurswiller sandstone deformed under a constant strain rate at an effective pressure of 10 MPa (a), and following deformation in the compaction regime (effective pressure = 80 MPa) up to axial strains of 1.5% (b), 3% (c), and 13% (d). A schematic sample drawing, highlighting the main features, is given next to each photograph; specific features are however difficult to distinguish on the sample taken to 13% strain due to the density of compaction bands.

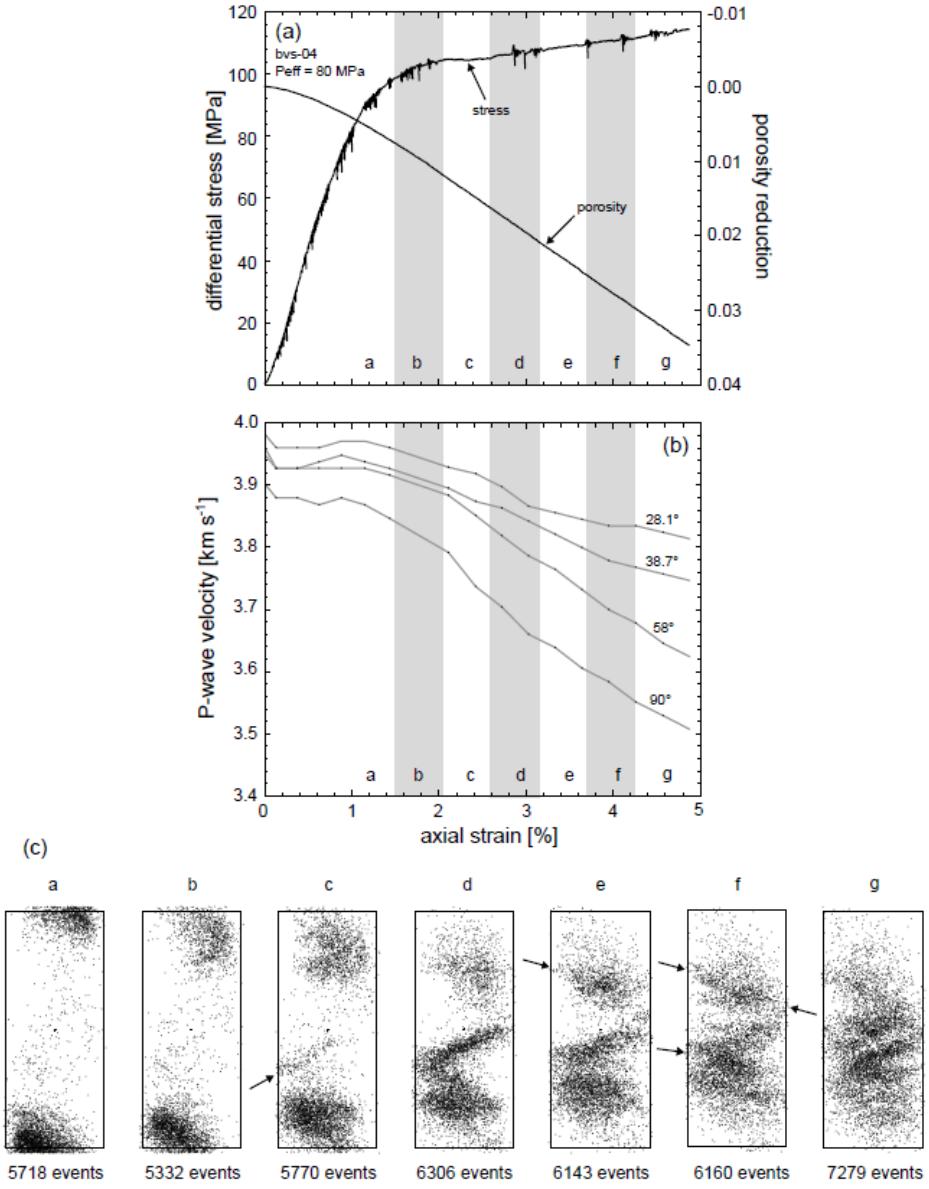

Figure 4. (a) Differential stress and porosity reduction as a function of axial strain for a constant strain rate experiment performed at an effective pressure of 80 MPa on a sample of Bleurswiller sandstone. (b) The evolution of P-wave speeds during the experiment shown in panel (a). The angle corresponds to the angle of the propagation direction relative to the sample axis. The strain intervals (a through to g) shown in panels (a) and (b) correspond to located acoustic emission events shown in panel (c). (c) Located acoustic emission events during the strain intervals shown in panels (a) and (b). Each rectangle represents the same cross-sectional slice in the middle of the cylindrical sample (40 mm in diameter and 100 mm in length). The arrows aid our description in the text (see text for details).

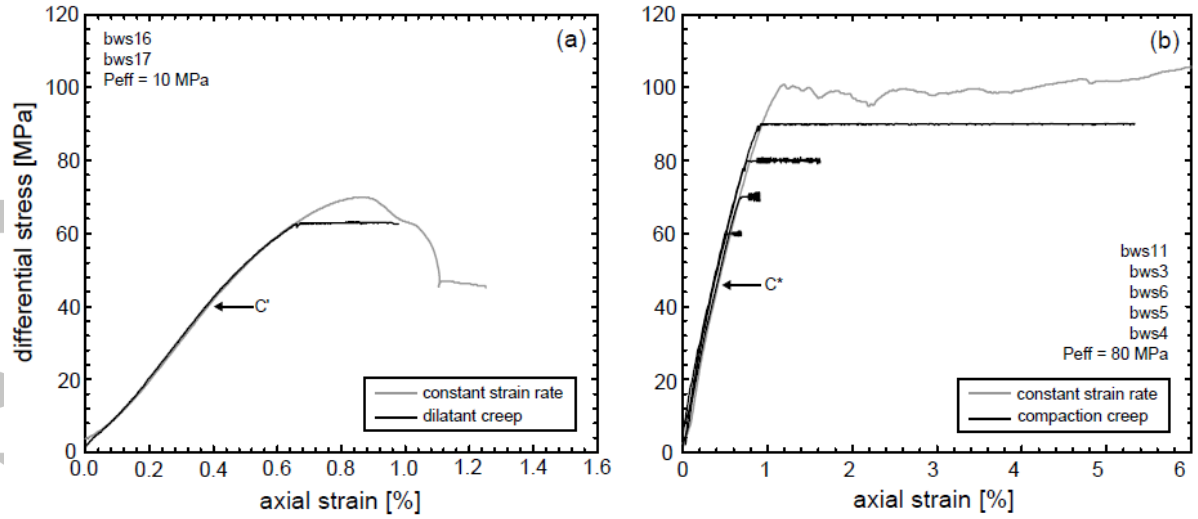

Figure 5. (a) Stress-strain curves for a constant strain rate (grey curve) and a constant stress (black curve) experiment performed on Bleurswiller sandstone at an effective pressure of 10 MPa. The onset of dilatational microcracking C' has been labelled (as in Figure 2). (b) Stress-strain curves for a constant strain rate (grey curve) experiment and multiple constant stress (black curves) experiments performed on Bleurswiller sandstone at an effective pressure of 80 MPa. The onset of shear-enhanced compaction C* has been labelled (as in Figure 2).

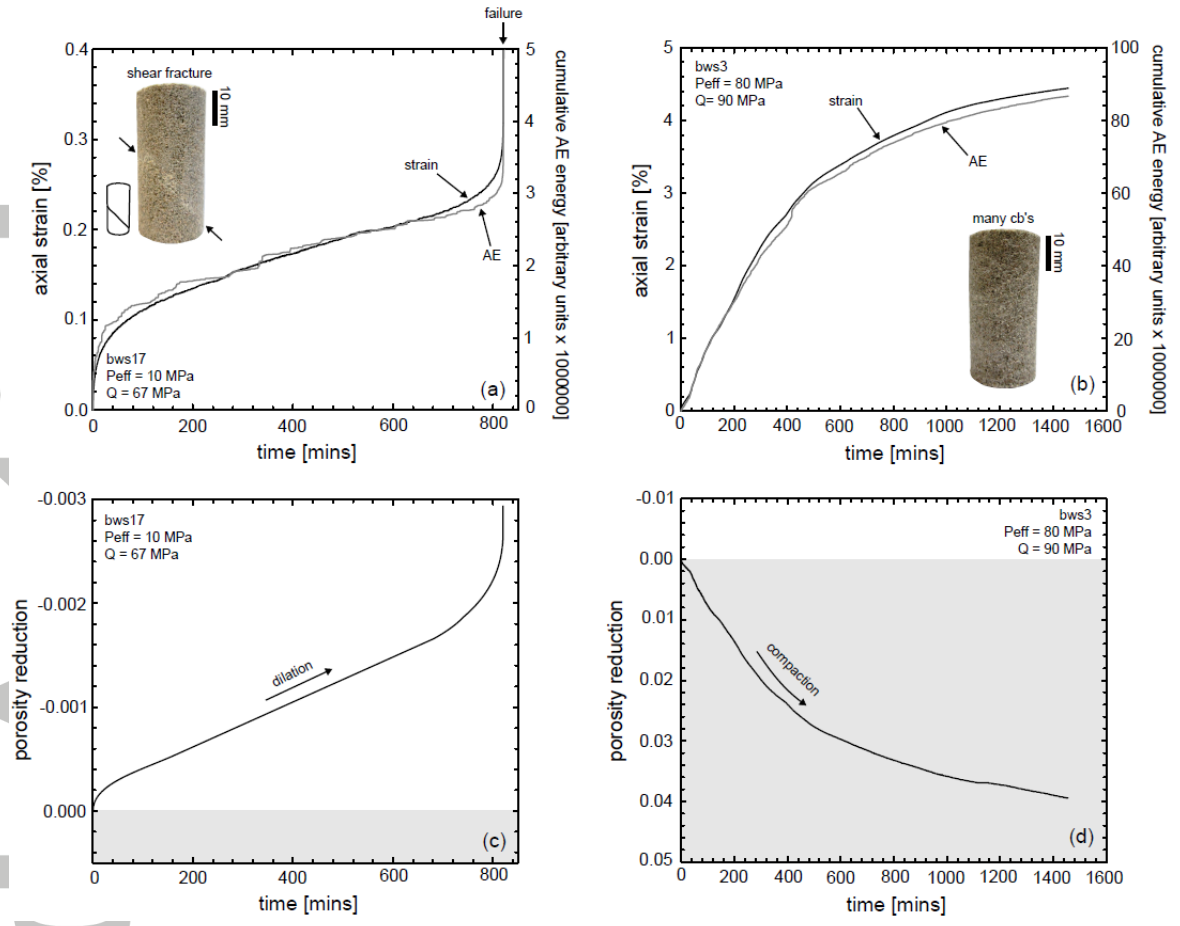

Figure 6. Bleurswiller sandstone constant stress experiments. (a) Axial strain and accumulative acoustic emission energy as a function of time (t = 0 corresponds to the start of the constant stress portion of the experiment) for a sample deformed in the dilatant regime (effective pressure = 10 MPa) at a constant stress of 67 MPa. Inset shows a photograph of the deformed sample and a schematic sample drawing highlighting the main features. (b) Axial strain and accumulative acoustic emission energy as a function of time (t = 0 corresponds to the start of the constant stress portion of the experiment) for a sample deformed in the compactant regime (effective pressure = 80 MPa) at a constant stress of 90 MPa. Inset shows a photograph of the deformed sample; due to the density of compaction bands, the specific features are difficult to represent on a schematic sample drawing. (c) The porosity reduction curve for the dilatant experiment shown in panel (a). The grey zone denotes the area of net compaction. (d) The porosity reduction curve for the compactant experiment shown in panel

(b). The grey zone denotes the area of net compaction. The large differences between the axes of the graphs exemplify the large differences between creep in the dilatant and compactant regimes.

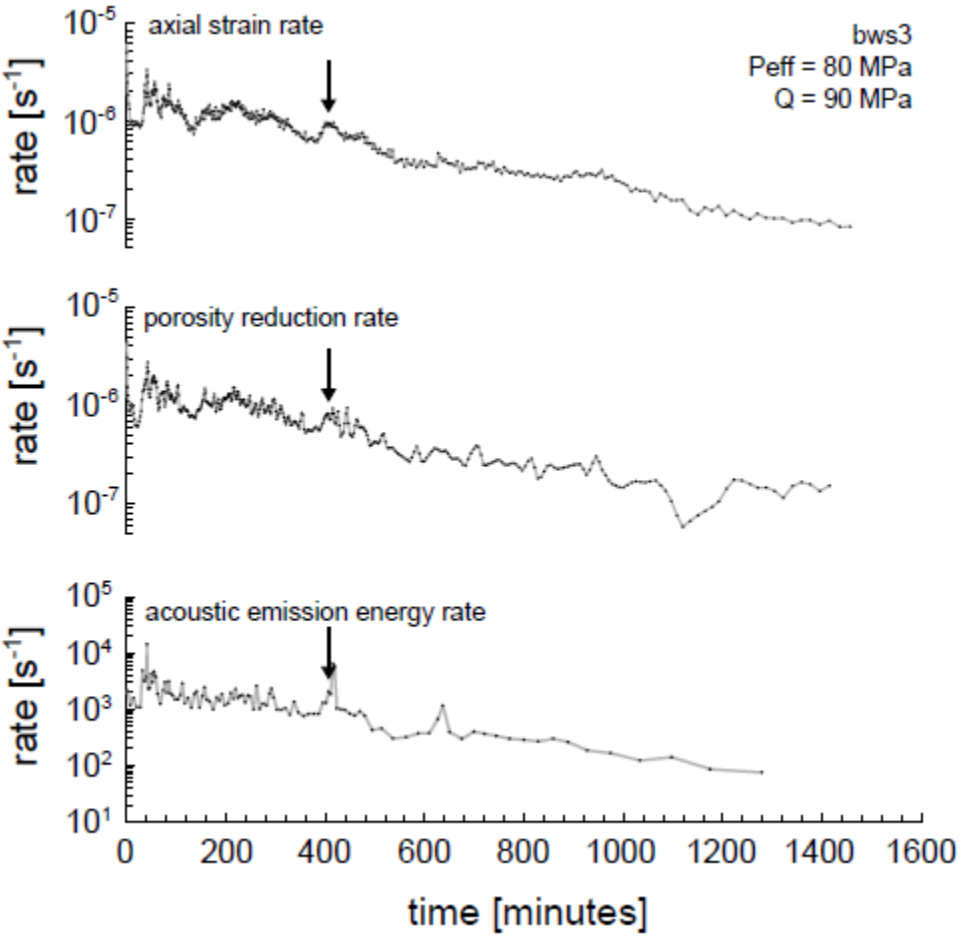

Figure 7. Rates of axial strain, porosity reduction, and acoustic emission energy against time (t = 0 corresponds to the start of the constant stress portion of the experiment) for a constant stress experiment performed on a sample of Bleurswiller sandstone in the compactant regime (effective pressure = 80 MPa; creep stress = 90 MPa). The data presented here are for the experiment shown in Figures 6b and 6d. An example of a higher rate excursion has been indicated with arrows.

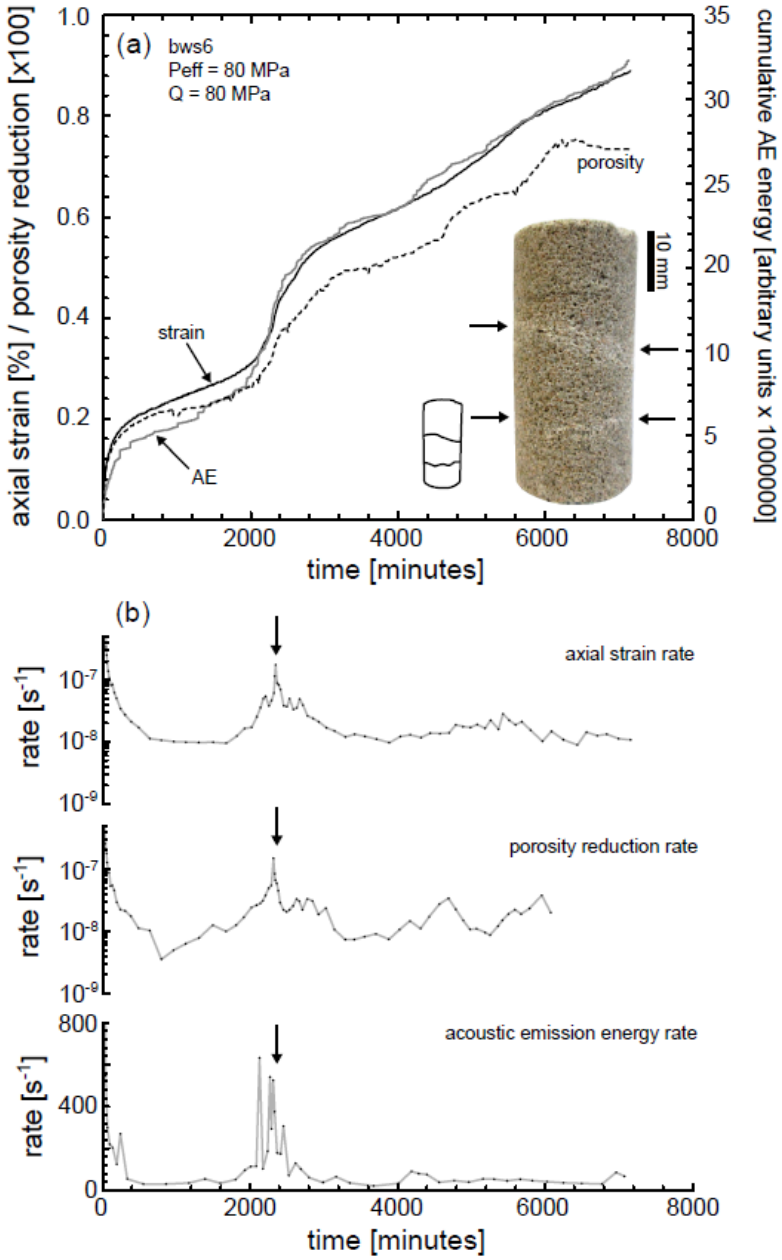

Figure 8. (a) Axial strain, porosity reduction, and accumulative acoustic emission energy as a function of time (t = 0 corresponds to the start of the constant stress portion of the experiment) for a sample of Bleurswiller sandstone deformed in the compactant regime (effective pressure = 80 MPa) at a constant stress of 80 MPa. Inset shows a photograph of the deformed sample and a schematic sample drawing highlighting the main features. (b) Rates of axial strain, porosity reduction, and acoustic emission energy as a function of time for the experiment shown in panel (a). An example of a higher rate excursion has been indicated with arrows.

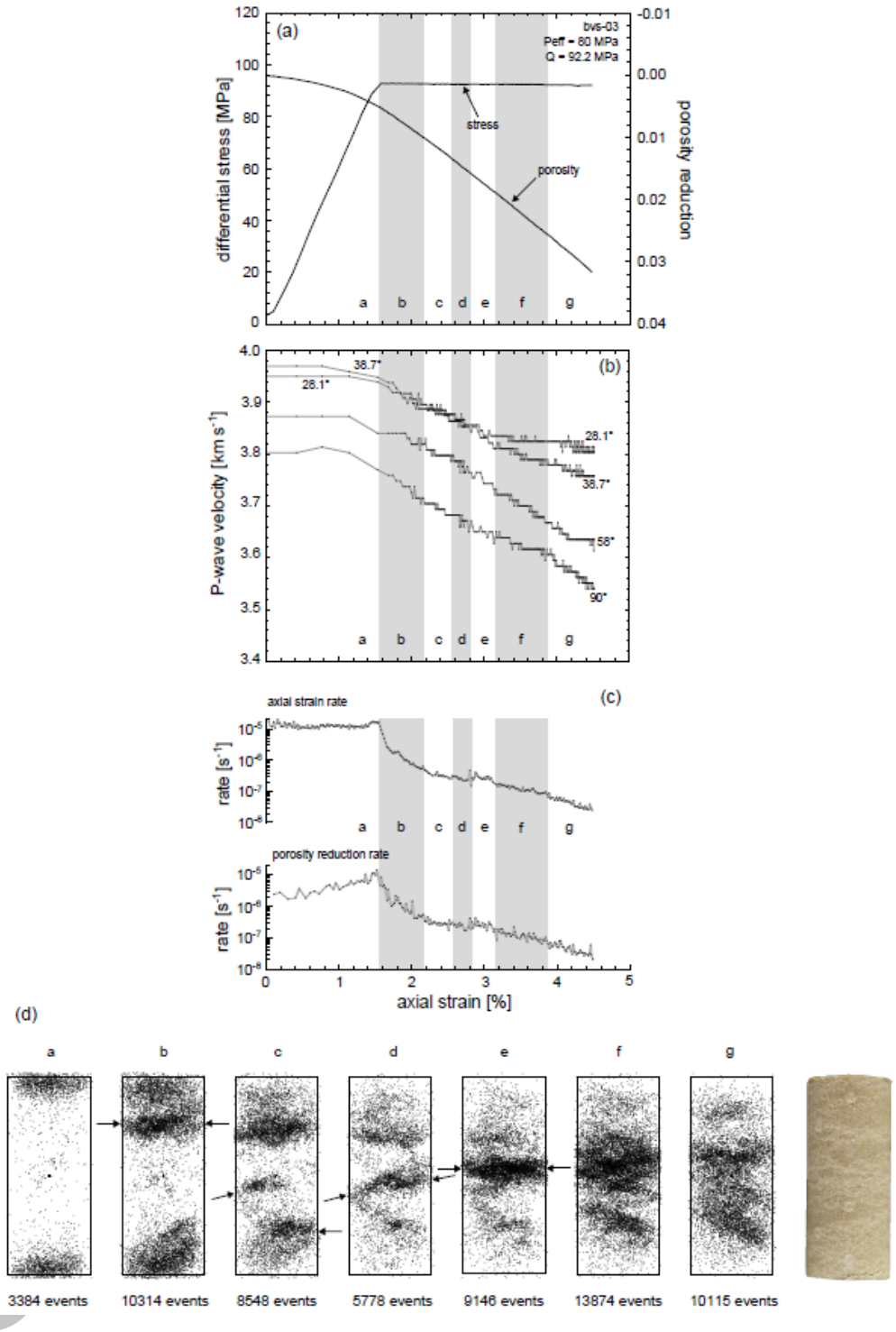

Figure 9. (a) Differential stress and porosity reduction as a function of axial strain for a constant stress (Q = 92.2 MPa) experiment performed at an effective pressure of 80 MPa on a sample of Bleurswiller sandstone. (b) The evolution of P-wave speeds during the experiment shown in panel (a). The angle corresponds to the angle of the propagation direction relative to the sample long axis. (c) Rates of axial strain and porosity reduction as a function of time for

the experiment shown in panel (a). The strain intervals (a through to g) shown in panels (a), (b), and (c) correspond to located acoustic emission events shown in panel (d). (d) Located acoustic emission events during the strain intervals shown in panels (a - c). Each rectangle represents the same cross-sectional slice in the middle of the cylindrical sample (40 mm in diameter and 100 mm in length). A photograph of the post-mortem sample is shown on the far right. The arrows aid our description in the text (see text for details).

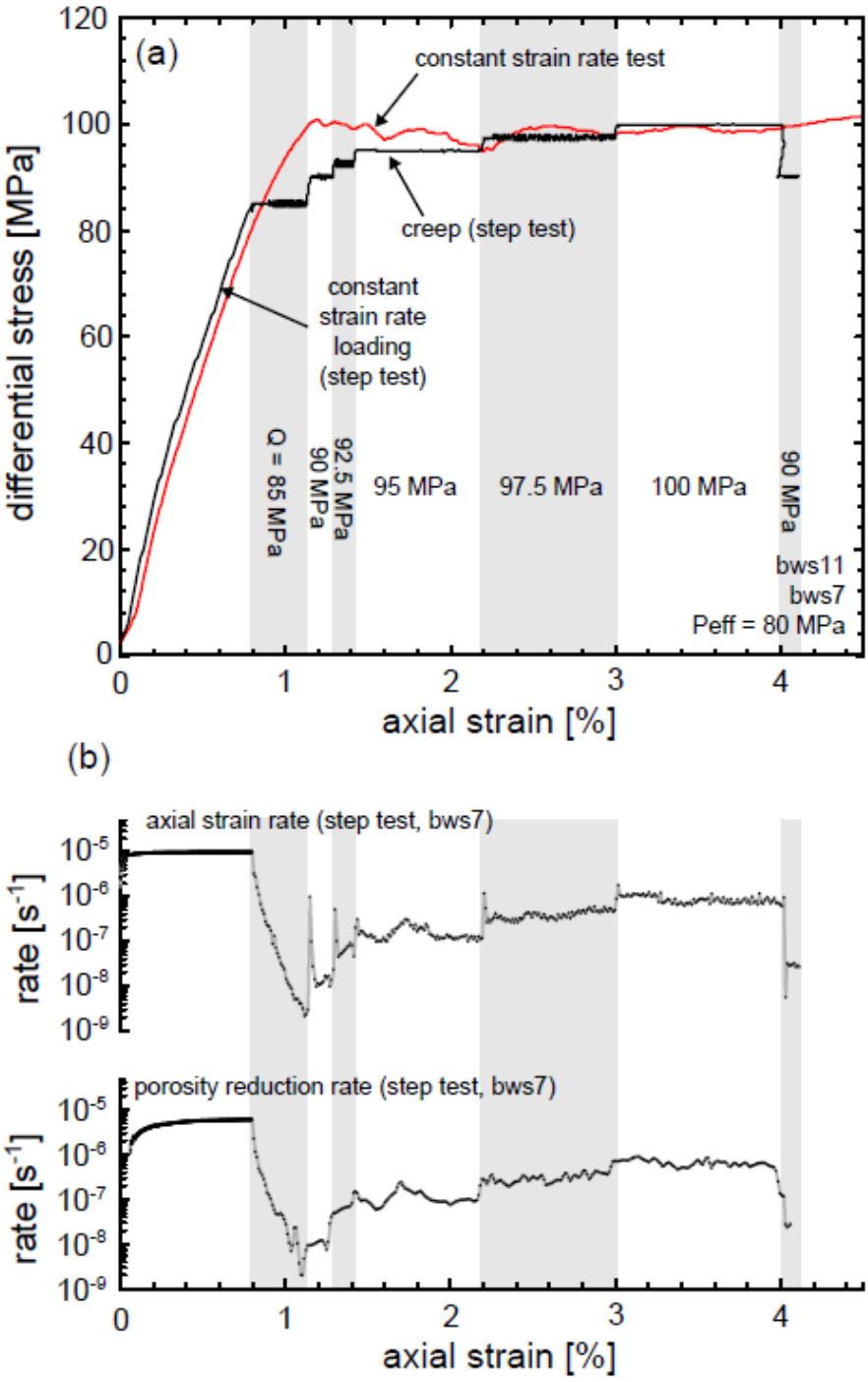

Figure 10. Stress-stepping creep experiment on Bleurswiller sandstone in the compactant regime. (a) Stress-strain curves for a constant strain rate experiment (red curve) and a stress-stepping creep experiment (black curve) performed at an effective pressure of 80 MPa. The values of creep stress for the each stress step are indicated on the figure. (b) Rates of axial strain and porosity reduction against strain for the stress-stepping creep experiment shown in panel (a).

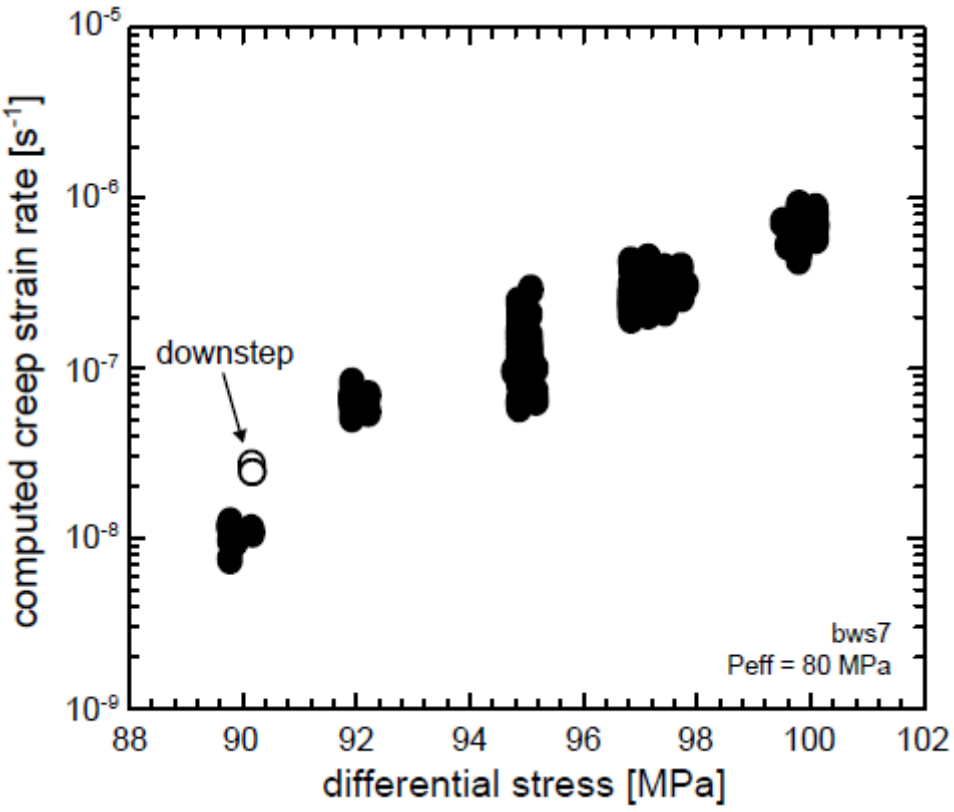

Figure 11. Stress-stepping creep strain rates in the compactant regime. The computed creep strain rates against differential stress during the stress-stepping creep experiment shown in Figure 10. The final step, for which the differential stress was reduced back to 90 MPa, is denoted by the unfilled circles.

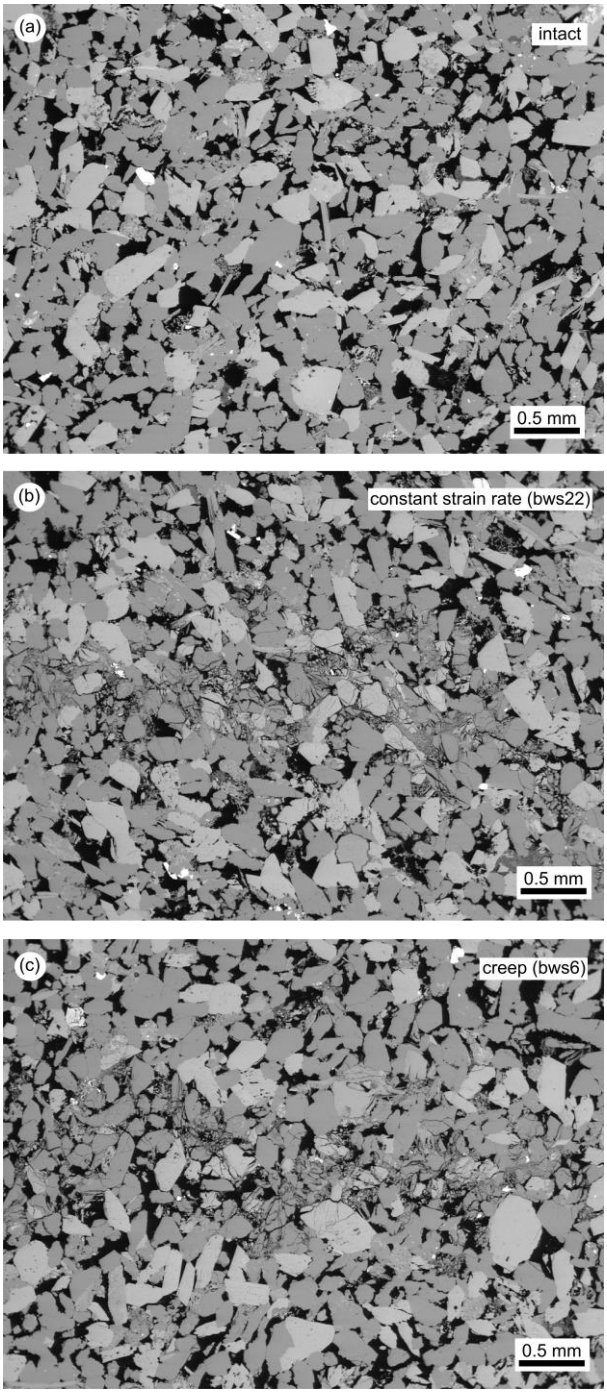

Figure 12. Microstructure. (a) Back scattered electron (BSE) photomicrograph of an undeformed sample of Bleurswiller sandstone. (b) BSE photomicrograph of a compaction band in a sample of Bleurswiller sandstone deformed under a constant strain rate (the compaction band runs from left to right in the center of the image). (c) BSE photomicrograph of a compaction band in a sample of Bleurswiller sandstone deformed under a constant stress (Q = 80 MPa) (the compaction band runs from left to right in the center of the image).

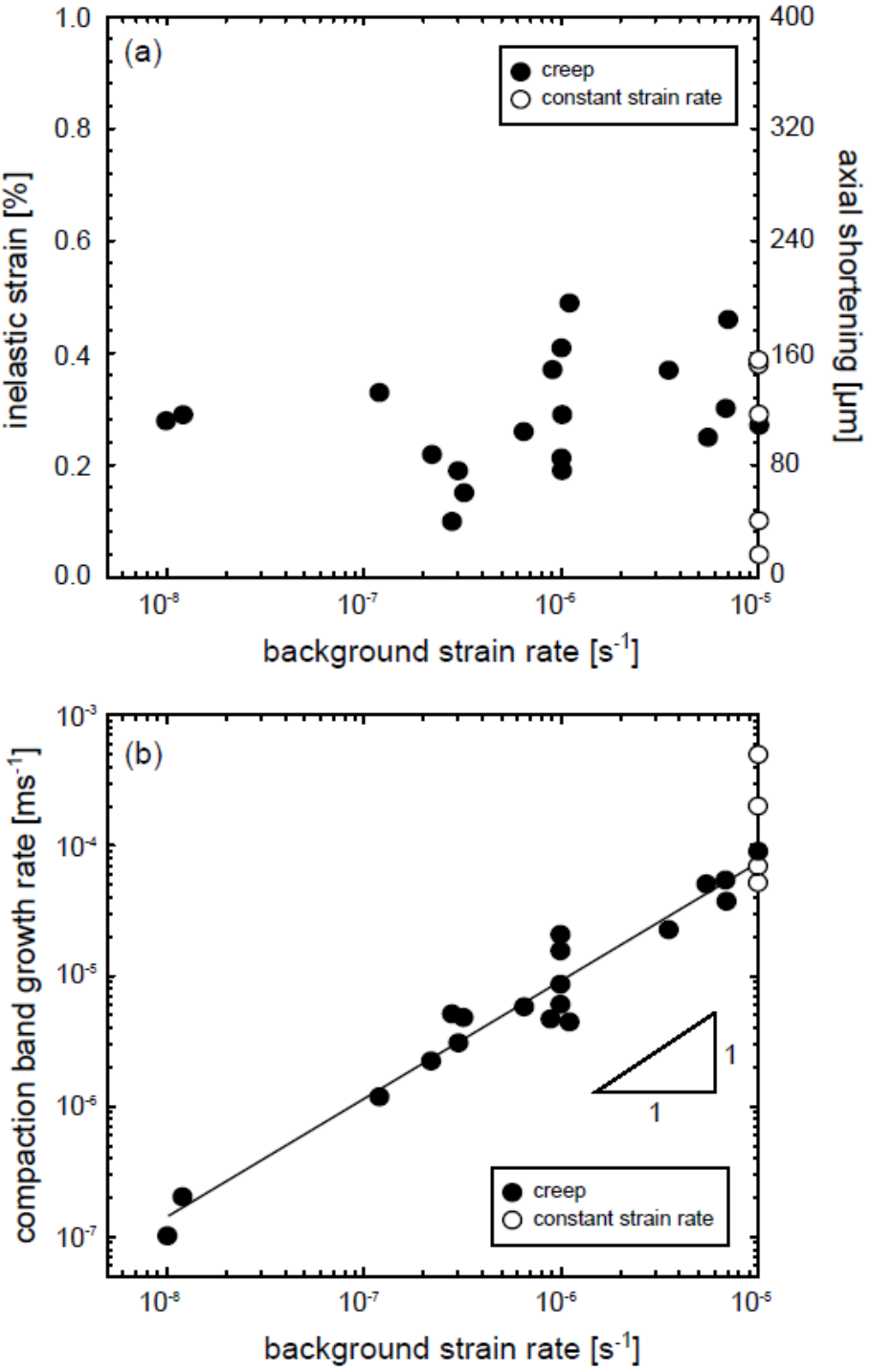

Figure 13. (a) The inelastic strain associated with the growth of a compaction band plotted as a function of the background strain rate for compaction bands formed under both constant stress (filled circles) and constant strain rate (unfilled circles) conditions. (b) The compaction band growth rate of bands formed under both constant stress (filled circles) and constant strain rate (unfilled circles) conditions plotted as a function of the background strain rate.

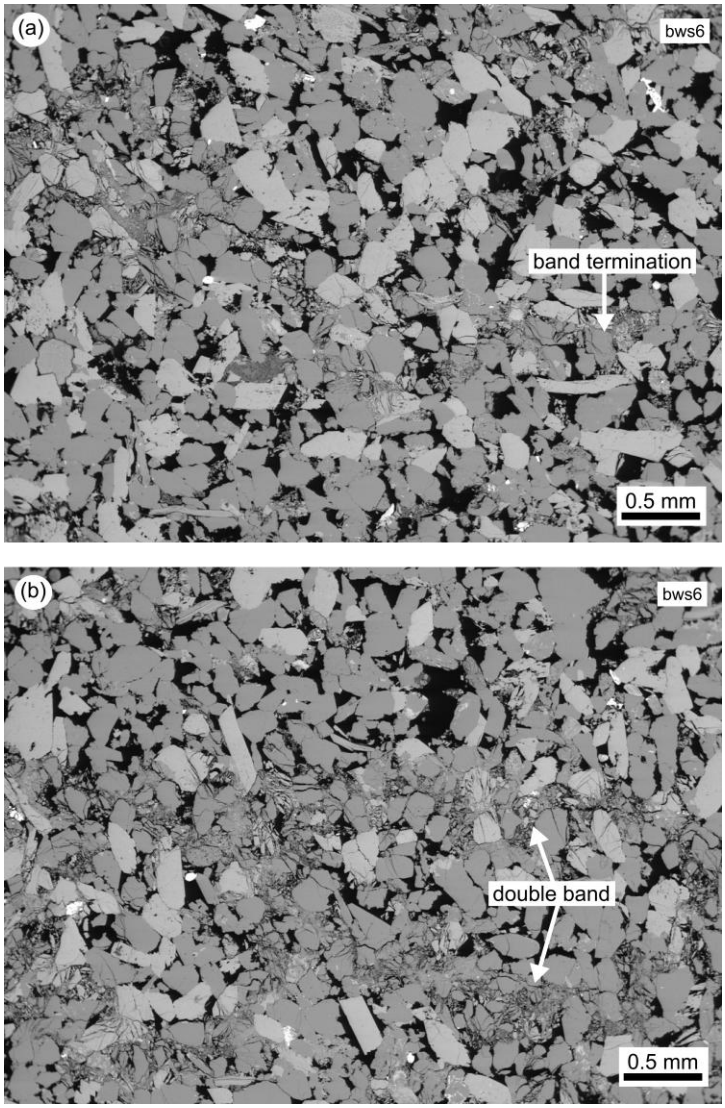

Figure 14. Complex compaction band geometrical attributes in Bleurswiller sandstone. (a) Back scattered electron (BSE) photomicrograph of a partial band (formed under a constant stress). (b) BSE photomicrograph of a band containing multiple strands (formed under a constant stress).

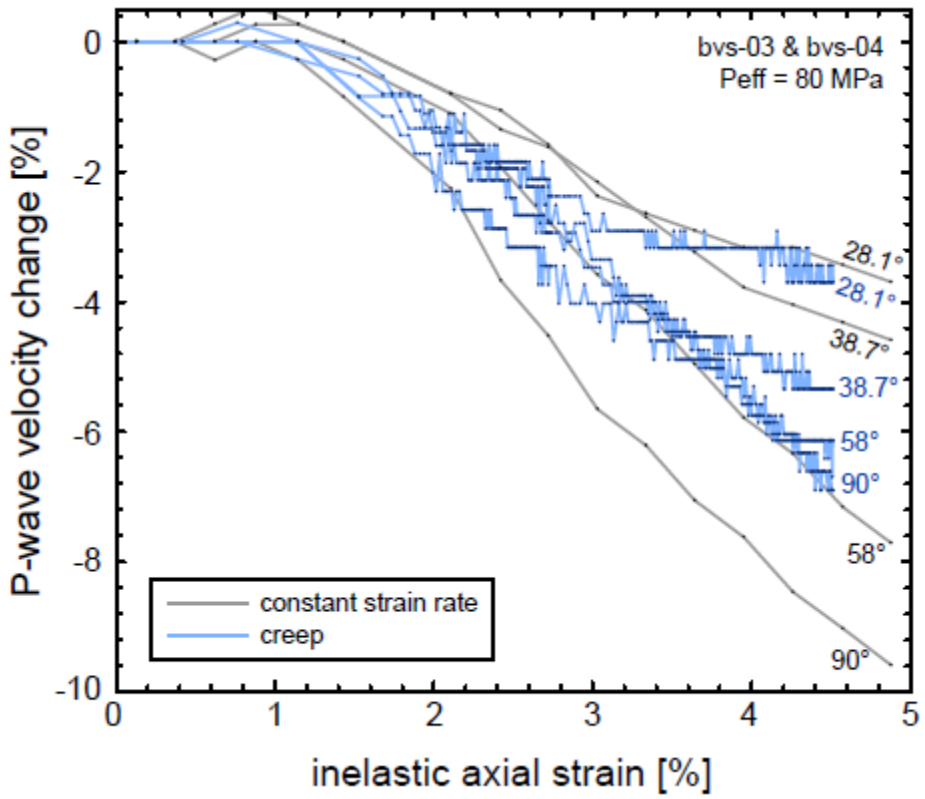

Figure 15. Relative evolution of P-wave speeds as a function inelastic axial strain for each propagation direction (normalized to their starting values) during a constant strain rate (grey curves) and a constant stress (blue curves) experiment performed on Bleurswiller sandstone at an effective pressure of 80 MPa. The angle corresponds to the angle of the propagation direction relative to the sample axis.

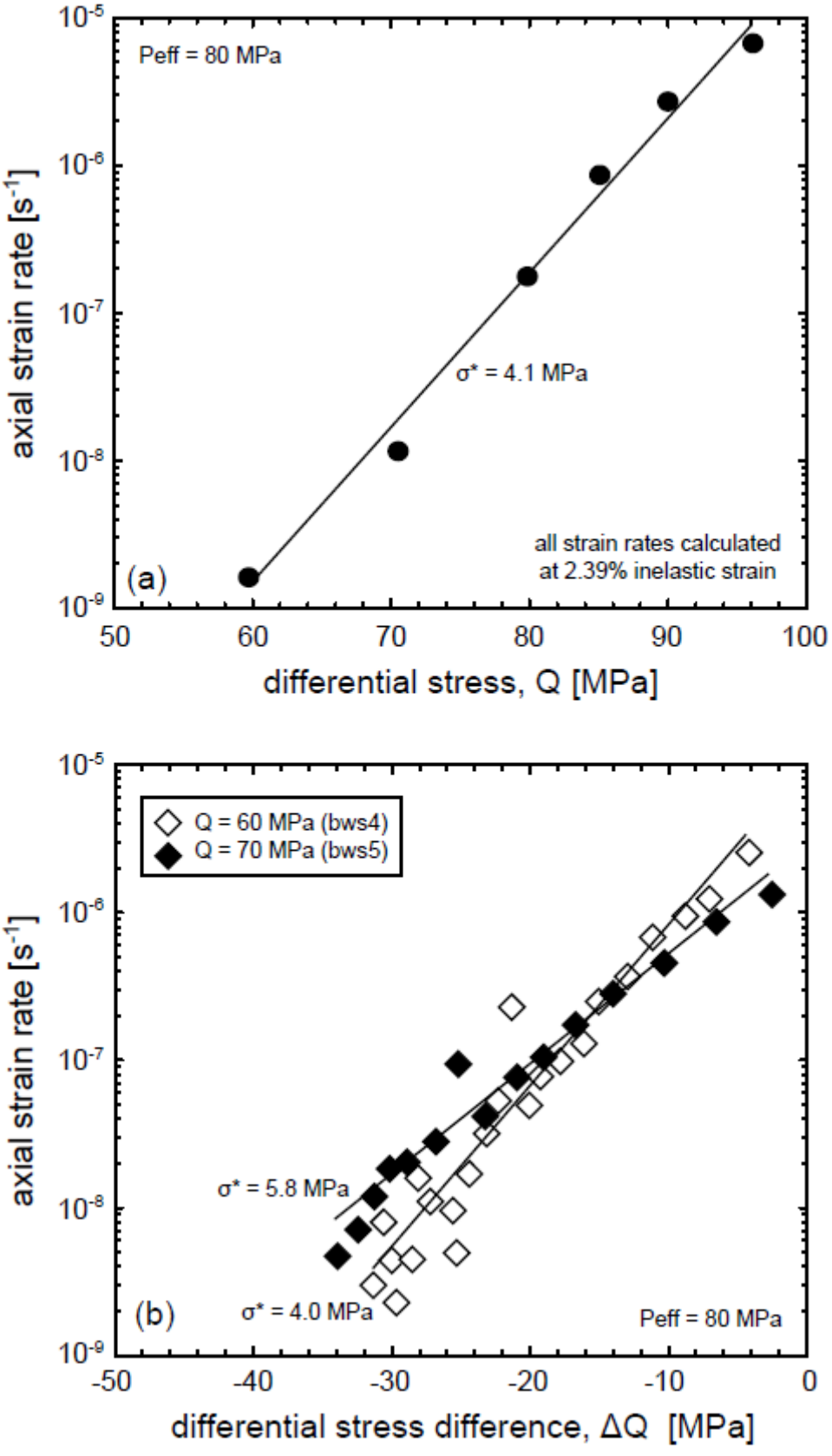

Figure 16. The stress-dependency of creep compaction. (a) Creep strain rates calculated at an inelastic strain of 2.39% for six creep experiments performed on Bleurswiller sandstone in

the compactant regime (effective pressure = 80 MPa) at differential creep stresses (60, 70, 80, 85, 90, and 97.5 MPa). The activation stress σ* value (see text for details) is provided for these data. (b) Creep strain rates as a function of differential stress difference ΔQ for two experiments performed on Bleurswiller sandstone in the compactant regime (effective pressure = 80 MPa) at different creep stresses of 60 (unfilled diamonds) and 70 MPa (filled diamonds). The activation stress σ* value (see text for details) is provided for both experiments.

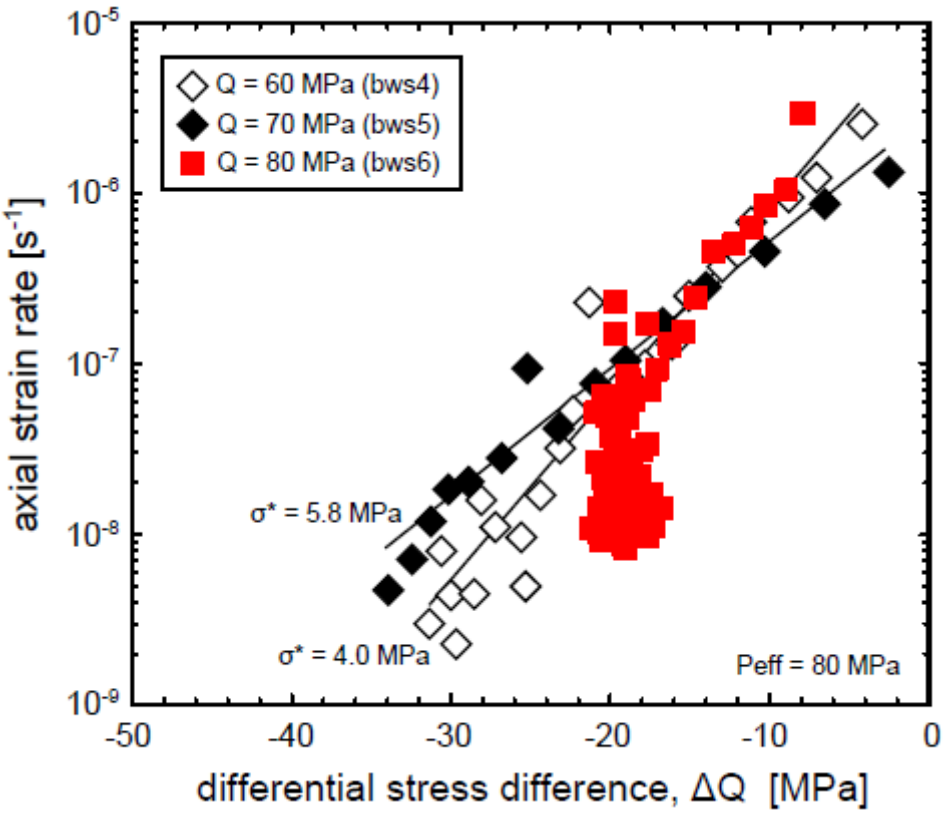

Figure 17. Creep strain rates as a function of differential stress difference ΔQ for three experiments performed on Bleurswiller sandstone in the compactant regime (effective pressure = 80 MPa). Two experiments (also shown in Figure 16) were performed at differential creep stresses of 60 and 70 MPa; the third (the red squares) was performed at a creep stress of 80 MPa. The activation stress σ* values (see text for details) are given for the experiments performed at creep stresses of 60 and 70 MPa.

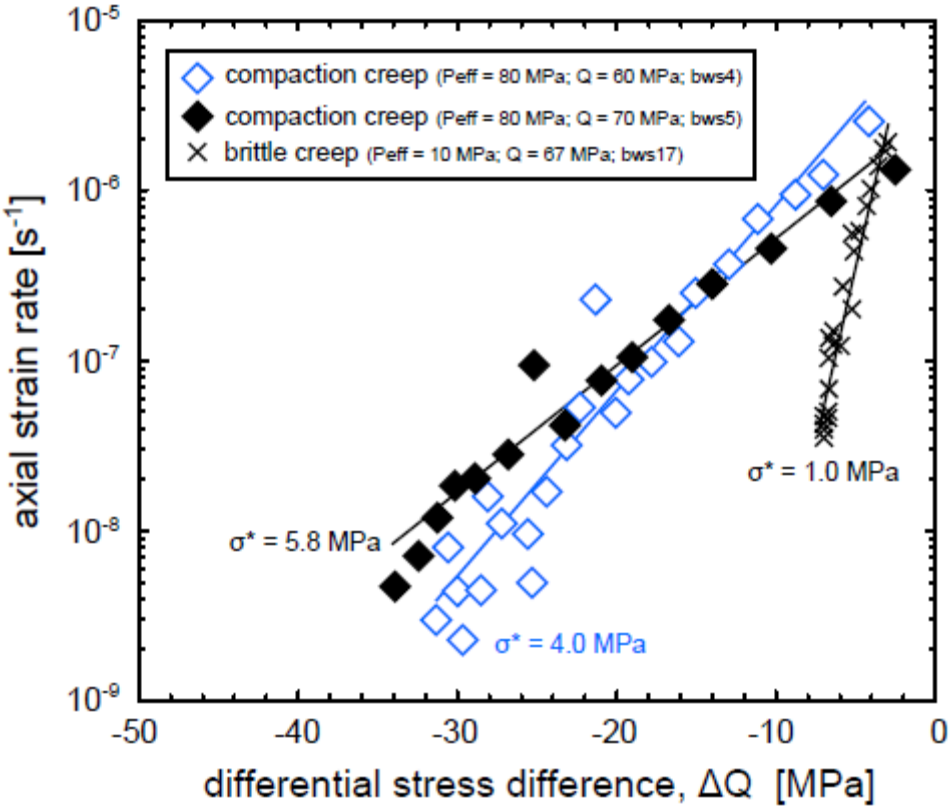

Figure 18. Creep strain rates as a function of differential stress difference ΔQ for two experiments performed in the compactant regime (effective pressure = 80 MPa; represented by filled and unfilled diamonds; also shown in Figures 16 and 17) and one experiment performed in the dilatant regime (effective pressure = 10 MPa; represented by crosses). Only the decelerating branch is shown for the dilatant experiment. The activation stress σ* values (see text for details) are given for each of the experiments.